CHALMERS
UNIVERSITY OF TECHNOLOGY

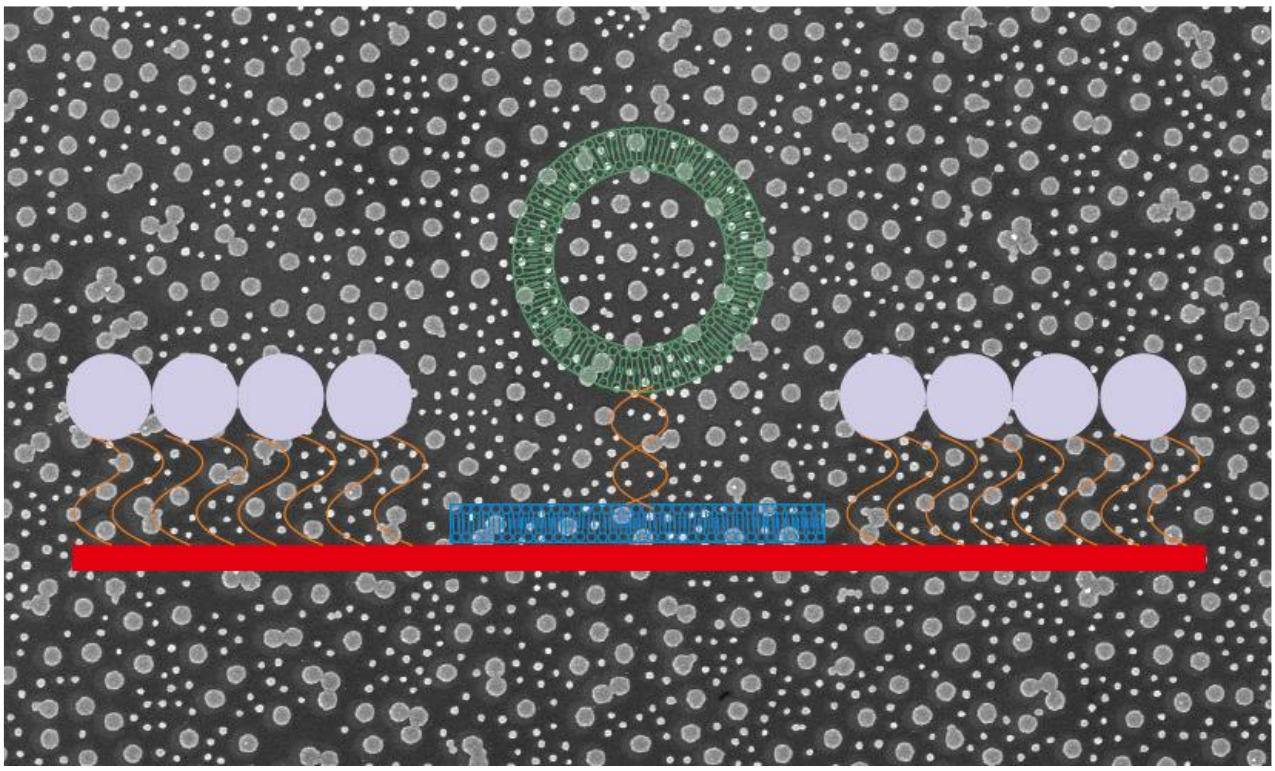

Biosensing with a dual-size plasmonic ruler

Master's thesis in nanotechnology

Viktor Axelsson

Department of Physics
CHALMERS UNIVERSITY OF TECHNOLOGY
Gothenburg, Sweden 2018

THESIS FOR THE DEGREE OF MASTER OF SCIENCE OF NANOTECHNOLOGY

Biosensing with a dual-size plasmonic ruler
Viktor Axelsson
Göteborg 2018

Supervisor: Ferry Nugroho, Chemical Physics
Examiner: Christoph Langhammer, Chemical Physics

Department of Physics
Chalmers University of Technology
SE-41296 Göteborg
Telephone +46 (0)31 772 1000

Cover photo: Schematics of the molecular systems studied on top of an SEM picture of the dual-size plasmonic sensor (ruler)

Imprint page photo: The sensor (ruler) and the plasmonic dual-peak extinction spectrum it produces

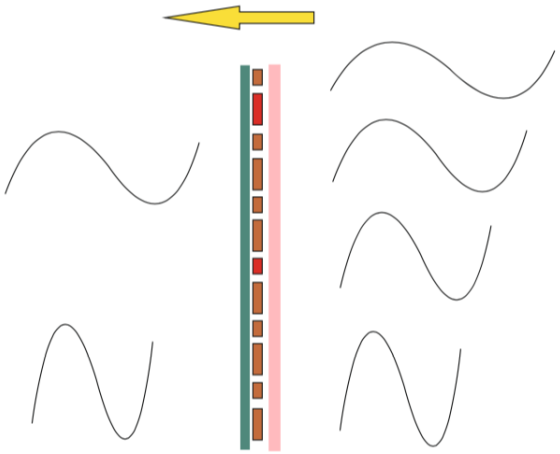

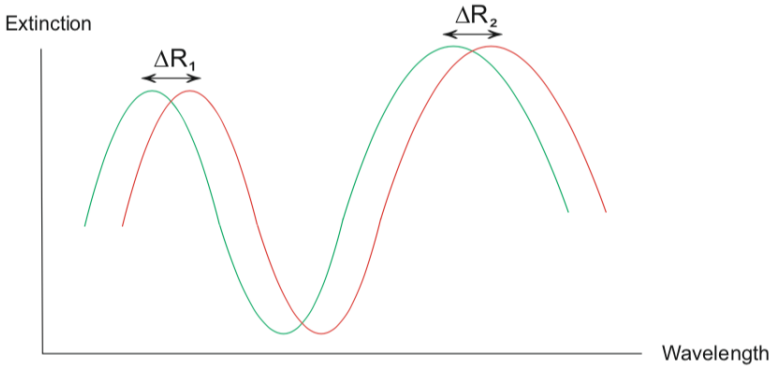

Abstract

Nanoplasmonic biosensing is a field of nanotechnology and plasmonics wherein localized surface plasmon resonance (LSPR) is utilized in order to detect and measure structures at the nanoscale. This detection is based upon the measurement of the shift of the LSPR peak as induced by the adsorption of the species studied. A nanoplasmonic sensor, comprised of silver nanodisks of two different sizes, as proposed and realised by the Langhammer Group at the department for Chemical Physics at Chalmers University of Technology, was used for the purpose of biosensing. The novel feature of this dual-size ruler is the determination of spatial dimension and refractive index of species adsorbed onto it, by virtue of taking the ratio of the LSPR shifts of the two peaks. Experiments were performed on two different molecular systems: 1-palmitoyl-2-oleoyl-sn-glycero-3-phosphocholine (POPC) with DNA and spherical lipid vesicles, and polylysine (PLL) with silica nanoparticles, with the goal being the determination of the thickness of a thin film composed of these compounds. The experimental results with respect to thickness determination were not solid, although a key configurational change of the POPC bilayer was clearly distinguished. This points at the ruler having the ability and resolution to record structural changes in lipid membranes, which indeed is one of it's visualized areas of application. In order to provide a solid proof-of-concept, a simpler molecular system should be studied, e.g. a spherically symmetrical nanoparticle deposited on top of POPC.

Acknowledgements

First and foremost I would like to extend my thanks to everyone at the divisions of Chemical Physics and Biological Physics, and especially those at the Langhammer group. Special thanks to Christoph for the opportunity and all the help, Ferry for your patience and guidance, Antonius for your kindness and assistance, and Iwan for enduring all my questions about USB2. Last but not least, I would like to thank my dear friend Harald for the well needed banter and laughter during long office days. To each and everyone of you, I say in the words of Vera Lynn: "We'll meet again, don't know where, don't know when, but I'm sure we'll meet again some sunny day."

Contents

1 Introduction

1.1 Background

Having a standard of measurement and being able to accurately determine lengths within that system is something we, inhabiting the macrocosmos of huge ensembles of molecules, take for granted. Admittedly, during the course of mankind, the possession of such a standard has not always been the case; as a standard unit of length, the metre was first accepted by a majority of the world's nations the year 1875 by the signing of a treaty in Paris[1]. Before that, a host of gauges existed before both within and between countries, and thus the problem lied in the definition of the length scale, a problem needed to be solved in order for the subsequent implementation of it in terms of physical measurements to be made possible. However, at the microscale, the scale nanotechnology is concerned with, there exists further problems. Agreeing to a standard of measurement is one thing, but here, instead, we struggle with making the actual *measurement*, which on the macroscale would translate to sticking your ruler to the table and register the length.

The power of length determination may be subtle, but is nonetheless impactful; a technologically sophisticated society need to be organised around an internally consistent system of measurement in order to allow for replication of creation and propagation of knowledge. For example; organising construction of buildings, analysing whether or not a child has a proper diet by monitoring its growth, and even more complex endeavours such as calculating fuel consumption of vehicles would not be available without the foundational techniques and standards of measurement.

Imagine, then, to have such a tool on the nanoscale. At this level, chemical and physical properties are heavily dependant on the size and shape of the system[2]. Examples of this dependency upon spatial configuration includes catalytic reaction selectivity[3][4], effects of molecular chain lengths in bio-nano interactions [5] and electric field emission properties[6]. One phenomenon that exhibits very interesting characteristics at the nanscale is the plasmon, discrete collections of oscillations of electrons in a material induced by light. Surface plasmons are plasmons that occur at the interface between two materials, and if this surface is planar, the excitation is called a surface plasmon polariton. However, if the surface is bounded, as it is in a particle, and the volume of said a particle is made so small that the wavelengths of the surface plasmons approach the particles dimensions, the excitation is called a localized surface plasmon (LSP)[7][8]. If such oscillatory modes can be excited by visible light, beautiful colours emerge, as can be seen in stained glass windows in, for example, old cathedrals or the Lycurgus cup, figure 1. These optical properties were first described by Gustav Mie in 1908 when he solved Maxwell's equations for the interaction of light with nanoparticles[9]. The colours are due to the nanoparticles absorbing the incoming light - an absorption that has it's maximum at what is known as the localized surface plasmon resonance (LSPR) frequency. The scientific field that have emerged from this, nanoplasmonics, now forms the basis for a lot of technology dedicated to sensing, especially biosensing[10]. Examples of plasmonic facilitated biosensing can be seen in [11], where recognition of specific biomolecules where achieved with nanopores, and [12], where the adsorption and specific binding kinetics of the avidin–biotinylated bovine serum albumin protein system was characterized. It is this field, nanoplasmonic biosensing, this thesis is concerned with.

When employing nanoplasmonic for biosensing one utilises the properties of LSPR. The absorption is, as stated, dependent upon the resonance frequency, and this frequency is in turn determined by the size and shape of the nanoparticle, as well as the refractive index of the surrounding medium [7]. Due to this, and the fact that the LSP is a surface phenomenon, molecules adsorbed onto the

Figure 1: The Lycurgus cup, exhibiting strong colouring due to plasmonic nanoparticles being integrated into the glass, source: wikimedia commons.

surface of the nanoparticle will change the resonance frequency. This shift of light frequencies that are absorbed due to changes in the nanoparticles' local environment is the basis for LSPR sensing. It is, however, not only the act of *detecting*, i.e. registering if something is there, that is of interest in this study, but rather - as introduced above - the act of *measuring*. How LSPR can be utilised in this regard will be explored, and a more detailed description, as well as mathematical formulations of plasmonics and it's role in biosensing, will be given in the theory section.

Nonetheless, there exists several other techniques apart from LSPR for sensing and measuring biomolecules and objects at the nanoscale. In the field of biology, for example, the length of DNA molecules can be determined through electrophoresis[13]. Electrophoresis, however, is known for it's often unsatisfactory precision. [14]. There has also been attempts at creating nanometer gauges using the deposition of thin films serving as reference objects[15], but such a setup is complicated and not at all suitable for all types of material considering one has to deposit and subsequently measure the reference in the very system one wants to analyse.

As a contrast, in [16] the authors used atomic layer deposition (ALD) to grow monolayers of aluminum oxide of known thickness on LSPR sensors consisting of Ag nanotriangles while monitoring the peak shifts, and through this correlated the shifts with the thickness of the film adsorbed. This made it possible to measure further film growth with atomic spatial resolution. This serves as proof of the high precision of *sensing* LSPR can achieve, but the results are nonetheless dependant upon the knowledge of the layers' thickness and can thus not be used independantly in order to measure a particle of unknown dimensions.

Now, we arrive at the more specific problem this thesis tries to adress; using LSPR sensors in order to, through a single experiment, determine the spatial dimensions and refractive index of an unknown species. This is to be achieved by finalizing and utilising the nanoplasmonic ruler visualised and developed by Christoph Langhammer, Ferry Nugroho and Padraic O'Reilly[17]. In this domain of study, what is most commonly used is a sensor comprised of homogeneous nanos-

tructures of one material[18][19] [20][21][22]. Having such a sensor allows one to get a response, a single peak, in the plasmonic extinction spectrum when some material is adsorbed onto it, but how much of this response is respectively due to the spatial dimensions or the refractive index is hard to tell. A single peak sensor is therefore not able to identify a completely unknown substance, but is reliant on either refractive index or dimensions being known beforehand. However, the concept has been further developed and a setup based upon two sources of information from the same system has been proposed and conducted[23]. What this means is that two different responses of the system, such as two different peaks in the extinction spectrum corresponding to two resonance frequencies, are monitored simultaneously and the ratio of said responses are converted into spatial dimension and refractive index. In such a setup, a plasmonic ruler is therefore more akin to a trip meter, being able to record, in real time, the length evolution of a system. A further analogy with a car can be made; being able to measure distance is one thing, but monitoring travelled distance as a function of time is what permits the correlation of the fuel consumption with specifics in the geography, i.e. the energy potential in which the car operates.

One can with a plasmonic ruler, thus, record the time evolution of the spatial dimensions and refractive index of a given system. Examples of what possibilities this uncovers includes conformational changes in biological membranes or organic structures due to changes in conditions such as temperature and pH, rate of growth of self-assembled systems and binding kinetics of ligands, to name a few[24]. The plasmonic ruler, therefore, does not only serve as a means for measurement, but also a method for gaining insight into other properties such as thermodynamics.

The dual-peak nanoplasmonic ruler this thesis is concerned with, as well as the creation of a mathematically determined system of equations for determining thickness and refractive index, will be explored more in-depth in the theory section. In figure 2, an SEM-image of Ag-nanoparticles of two different sizes as well as a plasmonic extinction spectrum produced by a sensor being comprised of such particles are shown.

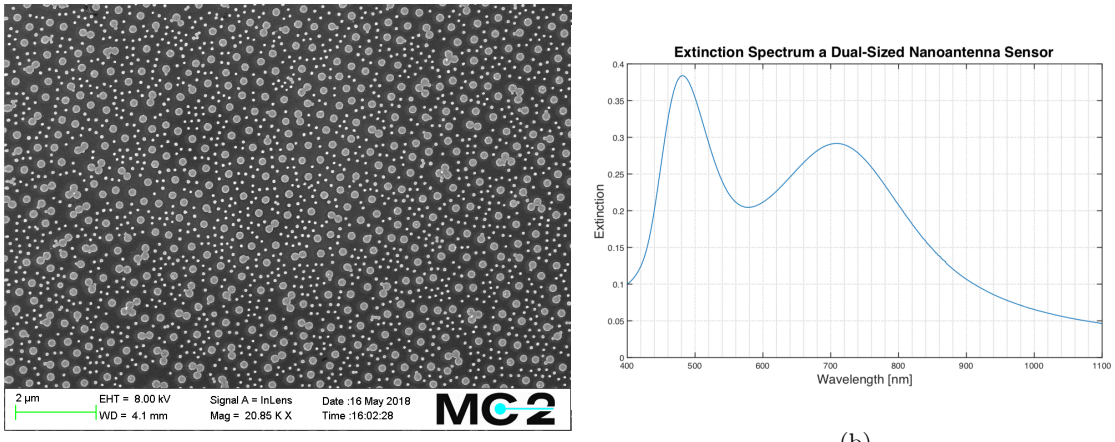

(a) (b)

Figure 2: a) An SEM-image of Ag-nanoparticles of two different sizes, 80 nm and 200 nm dispersed over a silica substrate. The dual-size sensor is comprised of such particles. b) A dual peak plasmonic extinction spectrum produced by the ruler.

1.2 Project Aim

This thesis aims at continuing previous work done in the Langhammer group, particularly that conducted by Padraic O'Reilly, on the development of a nanoplasmonic ruler[17]. The ruler is comprised of a surface on which arrays of silver (Ag) nanodisks of two different sizes are deposited. The nanodisks support LSPR, and it is through this phenomenon the environment is detected. Furthermore, the purpose of using nanodisks of two different sizes is to produce a plasmonic spectrum with two distinct and separate peaks. The relative shifts of these two peaks can be subsequently translated into thickness and refractive index of a medium normal to the sensor surface. This concept, the acquisition of the paramaters due to only one experiment on one sensor, is at the heart of what makes this device preferable over other techniques that are in need of calibrating the data by means of an external source such as QCM. The end goal of this ruler is to make sensing at a subnanoscale available - the sensing envisioned is primarily concerned with the determination of length of nanoparticles and biomolecules of said scale.

Determination of length is done by subjecting the plasmonic spectrum to change through the addition of a solution of interest. When the material one wants to study is deposited onto the ruler, it induces a shift in the LSPR-peaks, and it is this change that is correlated with the size and refractive index of said particles. The first molecular system studied in this project is 1-palmitoyl-2-oleoyl-sn-glycero-3-phosphocholine (POPC), ABCD-DNA - that may anchor to the POPC - and vesicles with a DNA complementary to the ABCD-DNA, which allows for them to bond. The second molecular system is polylysine (PLL) and silica microspheres (Polysciences Inc, PA, USA).

This thesis deals specifically with the demonstration of the dual-peak plasmonic ruler. This work is carried out with the Insplorion XNano system, in-house fabricated nanoplasmonic sensors and biomolecules. To demonstrate the usability of the plasmonic ruler, determination of the thickness and refractive index of the biomolecules is conducted.

2 Theory

2.1 LSPR-spectroscopy

The coherent collective oscillations of electrons in a material that would later be named plasmons where first described by David Pines and David Bohm in 1952[25]. In order to understand and describe this phenomenon, it is appropriate to adapt the free-electron model as developed by Arnold Sommerfeld[26], wherein the electrons in the conduction band are treated as a free-moving gas of negatively charged particles (hence the name) and the lattice as immobile, positive ions. When the electron gas is subjected to an external electric field, it will be perturbed as the electrons move in response to the applied field. This rearrangement results in a variation in the electron density, which at normal conditions are taken to be uniform in the free electron gas, where positive lattice ions are exposed. If the external field is removed, this charge separation will thus lead restoring force being exerted on the electron gas, see figure 3. The electrons are swung back but are not immediately relaxed, leading to an oscillatory motion. Photons, for example, induce a transient electric field in materials, and thus drives oscillatory movement of the electrons, which is why light is essential for plasmonics. This oscillatory motion has a resonance frequency, and it is this frequency that is probed by LSPR spectroscopy.

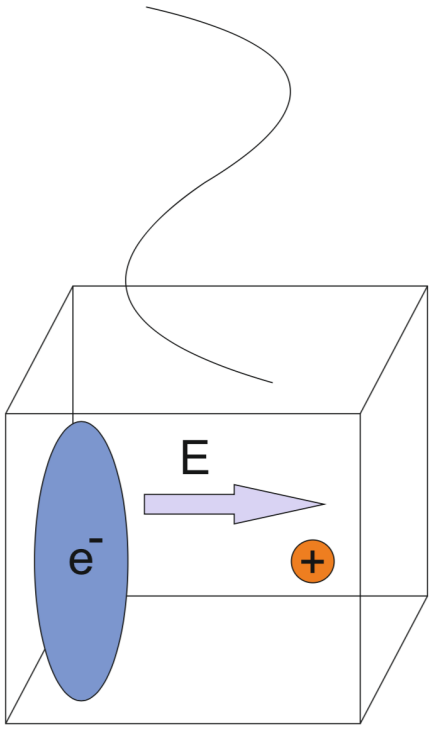

Figure 3: An external electric field induces a charge separation inside the slab of the material.

The aim of this section is to arrive at a quantitative expression that relates material properties, specifically the electrical permittivity, to the resonance frequency of the plasmon. Electrical permittivity is defined as the resistance that is encountered when an electeric field is formed within a medium, and it is thus a measure of a material's ability to *resist* the field, rather than what the name suggest; the contrary. Therefore, a high permittivity prevents internal fields to negate external fields. We will soon see how these properties are related. This derivation is based upon similar ones in [27], [28] and [29], which is mentioned here in order to avoid doing it multiple times

throughout the text.

First and foremost; the separation of charges due to an external electric field, as described above, gives rise to a dipole moment

$$\vec{\mu}(\omega) = -e\vec{r}(\omega) \tag{1}$$

This dipole moment is related to the displacement, r, of the electron. The displacement, then, can be described by the function of the movement of the electron in this internal electric field created by seperation of charges

$$m_e \frac{\partial^2 \vec{r}}{\partial t^2} + m_e \Gamma \frac{\partial \vec{r}}{\partial t} + m_e \omega_0^2 \vec{r} = -e\vec{E}(\vec{r}, t) \tag{2}$$

where the first term represents the acceleration due to the field, the second term a frictional force (Γ is a dampening factor due to the electron scattering off other electrons and the lattice), and the third a restoring force exerted on the electron by the positive atomic nucleus (ω_0 is the frequency of this force). Keep in mind that the right hand side is the *net* electric field acting on the electron, and thus not the pure applied field, although they are related and dependant on the same variable.

Considering that the displacement in (1) is a function of frequency, it is in that domain that we wish to express the dipole moment as a function of the net internal electric field. We therefore take the Fourier transform of (2), do some rearranging, and have the expression for the displacement as a function of frequency

$$\vec{r}(\omega) = \frac{-e}{m_e} \frac{\vec{E}(\omega)}{(-\omega^2 - \Gamma i\omega + \omega_0^2)} \tag{3}$$

By substituting (3) into (1)

$$\vec{\mu}(\omega) = \frac{e}{m_e} \frac{\vec{E}(\omega)}{(-\omega^2 - \Gamma i\omega + \omega_0^2)} \tag{4}$$

we have the relationship between the dipole moment induced in the material and the internal electric field. To further investigate how the material properties are related to the plasmon frequency, polarizability, a material's *inclination* to form dipoles, must be regarded. The polarization of a material, as related to the electric field driving it, is expressed as

$$\vec{P}(\omega) = \epsilon_0 \chi(\omega) \vec{E}(\omega) \tag{5}$$

where ϵ_0 is the electrical permittivity in free space and $\chi(\omega)$ the electrical susceptibility, a proportionality constant that dictates the amount of polarization, i.e. the amount of dipoles, induced in the material. Therefore, the polarization can also be expressed in terms of a number of dipoles

$$\vec{P}(\omega) = N\vec{\mu}(\omega) \tag{6}$$

Combining (6) and (5), we get

$$\chi(\omega) = \frac{N\vec{\mu}(\omega)}{\epsilon_0 \vec{E}(\omega)} \tag{7}$$

and by using (4), we arrive at

$$\chi(\omega) = \frac{Ne^2}{m_e \epsilon_0} \frac{1}{(-\omega^2 - \Gamma i\omega + \omega_0^2)} \tag{8}$$

Now, it so happens that the frequency at which the electrons oscillate, the so-called *plasma frequency*, is defined as

$$\omega_p = \sqrt{\frac{Ne^2}{m_e \epsilon_0}} \tag{9}$$

We therefore arrive at an interesting relationship between a material's electric susceptibility and the frequency of it's plasmons

$$\chi(\omega) = \frac{\omega_p^2}{-\omega^2 - \Gamma i\omega + \omega_0^2} \tag{10}$$

From here, relating ω_p to the electrical permittivity is relatively straightforward. The electric susceptibility, χ, can be expressed in terms of the relative electric permittivity, ϵ_r, of the material

$$\chi(\omega) = \epsilon_r - 1 \tag{11}$$

Together with (10), we have:

$$\epsilon_r = 1 + \frac{\omega_p^2}{-\omega^2 - \Gamma i\omega + \omega_0^2} \tag{12}$$

In order to proceed from here, we need some simplifications. As mentioned above, the employement of the free electron model entails electrons that are unaffected by the ionic lattice, which is why we can omit ω_0, the frequency of this binding potential. The relative permittivity, or dielectric function, is thus

$$\epsilon_r = 1 - \frac{\omega_p^2}{\omega^2 + \Gamma i\omega} \tag{13}$$

In order to further study this expression, we need to separate the real part from the imaginary. By multiplying both numerator and denominator in the second term in (13) by the complex conjugate of the denominator, and after some rearranging, we arrive at the expressions

$$\epsilon_r^R = 1 - \frac{\omega_p^2}{\omega^2 + \Gamma^2} \tag{14}$$

$$\epsilon_r^I = \frac{\omega_p^2 \Gamma}{\omega^3 + \Gamma^2 \omega} \tag{15}$$

where ϵ_r^R is the real part and ϵ_r^I the imaginary. Here we focus on the real part, since the imaginary is related to the decay of electric fields in the medium rather than the absolute strength of it. Furthermore, (14) and (15) can both simplified by noting that the damping factor, Γ, is for visible light about hundred times smaller than the frequency of said light[17]. We therefore arrive at

$$\epsilon_r^R = 1 - \frac{\omega_p^2}{\omega^2} \tag{16}$$

$$\epsilon_r^I = \frac{\omega_p^2 \Gamma}{\omega^3} \tag{17}$$

and we finally have a comprehensive, manageable relation between the electric permittivity, the frequency of the light that applies the external electric field and the frequency of the plasmons of the material. When the frequency of the external field, ω is large and approaches the plasma frequency, ω_p, the electric permittivity is predominantly real, and can be approximated by (16)[27]. If $\omega > \omega_p$, the permittivity is large, i.e. the ability of the material to form internal fields in order to negate the external field is low, and the field is transmitted through the material. On the other hand, if $\omega < \omega_p$, internal fields are easily formed and an external field is reflected. At the plasma frequency, however, the plasmons are put into resonance. The nature of this resonance condition will be more clear later.

Now imagine that the dimensions in figure 3 approach the nanoscale, and the slab becomes a nanoparticle. As stated in the introduction, the surface polariton, the coupling of an electromagnetic wave and oscillations of electrons, is termed a localized surface plasmon for a small particle of that size. The word *localized* refers to the fact that the plasmon is confined in space, in this case the volume of the particle, and this nanolocalization of optical energy is what at the heart of nanoplasmonics[30]. An evanescent field up to 200nm from surface of particle [31] is formed, and it is disturbances in this field, which in turn affects the oscillation frequency of the electrons in the particle, that makes sensing possible, as we will soon see.

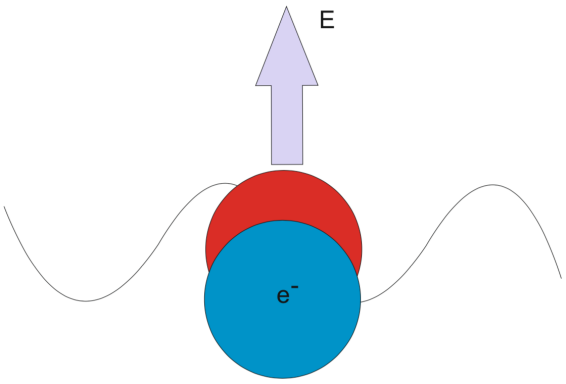

Figure 4: A nanoparticle interacting with light of wavelength similar to the dimensions of the particle. The electric field displaces the electrons in the particle, and the negative electron cloud thus start to oscillate around the stationary lattice ions.

The plasmon resonance, as described above, occurs when the frequency of the incoming light matches that of the particle plasmon. This is schematically illustrated in figure 4. Resonance entails maximized oscillations, which in turn implies maximized dipole moments. With this line of

thought, it is appropriate to consider the property of polarizability; the tendency of the material to form dipoles. A way of conceptualizing the resonance, then, is considering the state in which the polarizability is at it's maximum. Polarizability is defined as

$$\alpha = \frac{\epsilon_0}{N}\chi \tag{18}$$

where χ, as stated above, is the electric susceptibility. Combine this with (11)

$$\alpha = \frac{\epsilon_0}{N}(\epsilon_r - 1) \tag{19}$$

The polarizability is related to polarization, $\vec{P}$, through

$$\vec{P} = \alpha\vec{E} \tag{20}$$

as given by (5) and (18), where $\vec{E}$ is the net field driving the plasmon. This field, however, is not the same as the external field, that belonging to the photon, but related through

$$\vec{E} = \frac{\vec{E_0}}{\epsilon_r} \tag{21}$$

where $\vec{E_0}$ is the external, applied field. It is this field we want to consider when utilising plasmonics for the purpose of sensing, since it is this field that may be perturbed by the medium surrounding a plasmonic particle.

Combining (19), (20) and (21) gives us

$$\vec{P} = \epsilon_0(\epsilon_r - 1)\frac{\vec{E_0}}{\epsilon_r} \tag{22}$$

And from this, the relation

$$\alpha = \frac{\epsilon_0(\epsilon_r - 1)}{\epsilon_r} \tag{23}$$

can be acquired. This relationship between the polarizability - the tendency for the nanoparticle to form dipoles and thus for the plasmon to oscillate - and the electric permittivity shines light onto why the resonance is achieved when ϵ_r approaches zero, as it does when the frequency of the electric field is equal to the plasmon frequency, since (23) then goes to infinity.

We have now established, through (16) and (23), the formulas that describe the resonance condition. (23) was derived through the perspective of the external field, but in order to gain insight into how the surroundings interact with a nanoparticle and it's plasmonic properties, we must somehow link this expression with the properties of the medium around said particle. In the case of a slab of macroscopic dimensions, where an interface between the plasmonic material and the surrounding dielectric medium can be said to be planar, the surface charge distribution produced as a consequence of polarization does not yield a field outside the plasmonic material. The change in *geometry* when the material becomes a nanoparticle, however, gives rise to the aforementioned

evanescent field; this emerging phenomenon constitutes an example of qualitative differences between the macro-and nanoscale [28].

The net electric field inside our small particle is given by

$$\vec{E} = \vec{E_1} - L\frac{\vec{P}}{\epsilon_0 \epsilon_1} \tag{24}$$

Where ϵ_1 is the permittivity of the surrounding medium, and $\vec{E_1}$ is now the field in the surrounding medium and L is a shaping factor with a value range of $1/3 - 1$. By employing (5) for the net polarization, $\vec{P}$, inside the particle and substitute (24) into (5), we get, after some rearranging

$$\vec{P} = \epsilon_0 \frac{\chi \vec{E_1}}{1 + \frac{L\chi}{\epsilon_1}} \tag{25}$$

Here, χ is the *net* electric susceptibility of the particle, and can be rewritten as

$$\chi = \chi_2 - \chi_1 = \epsilon_2 - \epsilon_1 \tag{26}$$

where ϵ_2 is the permittivity of the particle. Together with (11), we have for the net polarization of the particle

$$\vec{P} = \epsilon_0(\epsilon_2 - \epsilon_1)\frac{\epsilon_1 \vec{E_1}}{\epsilon_1 + L(\epsilon_2 - \epsilon_1)} \tag{27}$$

By once again using (20), the polarizability of the plasmonic nanoparticle is found

$$\alpha = V\frac{\epsilon_0 \epsilon_1(\epsilon_2 - \epsilon_1)}{\epsilon_1 + L(\epsilon_2 - \epsilon_1)} \tag{28}$$

where V is the volume of the particle, since the polarizibility is derived on the basis of per unit volume. Returning to the discussion about the resonance condition; as stated before, resonance occur when the denominator in the polarizability is zero. For spherical particles, the shaping factor L is 1/3, and substituting this in (28) and putting the denominator to zero, we arrive at the relation

$$\epsilon_2 = -2\epsilon_1 \tag{29}$$

and substituting this into (16)

$$-2\epsilon_1 = 1 - \frac{\omega_p^2}{\omega^2} \tag{30}$$

Here, we have finally produced a formula that, given the free-electron model assumptions, relate the electric permittivity, i.e. a material property, of the surrounding medium to the plasmon resonance frequency

$$\omega_{LSPR} = \frac{\omega_p}{\sqrt{1 + 2\epsilon_1}} \tag{31}$$

This frequency at which localized surface plasmon resonance occur due to attenuation by a surrounding medium. It is this powerful relationship that provides us with the mathematical core directly linking a nanoparticles local environment to it's optical properties, and lays the foundation for plasmonic sensing, which is explored more in-depth in the next subsection.

2.2 Biosensing and the nanoplasmonic ruler

(31) was derived with the assumption that the nanoparticle was of spherical shape. However, as is clearly visible, the frequency at which LSPR occurs for such a particle is dependent on the shaping factor L, since the shape determines the charge distribution and therefore the evanescent field around the particle.

Geometry, as has already been stated, is key. The presence of such a clear connection between a nanoparticle's spatial configuration and optical properties provides a tool for shaping the plasmonic material for the system one wants to study - the engineer's dream. Figure 5 depicts this connection. It is in this rather playful domain the great potential of plasmonics in biosensing lies. By shaping the chemical and physical properties of one's sensor[32], one can, for example, tweak the particle in such a way as to to fit the optical properties into a window necessary for that field of study, such as the infrared region in the case of in vivo studies[33][34], or design a system in which light of a non-destructive frequency can be used to sense molecules that would otherwise be destroyed. Shape is indeed also one of the main strategies employed when producing more sensitive sensors[35] - sensitivity being an important parameter discussed later on in this report. Furthermore; specific shapes can, in an inhomogeneous ensemble of nanoparticles, be distinguished from one another, leading to possibilites of using plasmonic particles as markers or probes[36]. The facilitation of optical waveguides based upon how the plasmon modes couple as a function of geometry has also been pursued[37], as well as the improvement of the efficiency of optical trapping by nanoparticles[38].

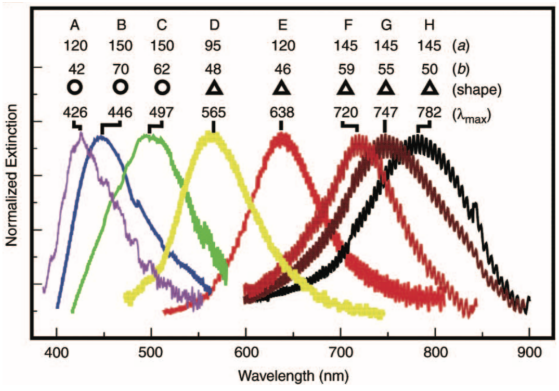

(a)

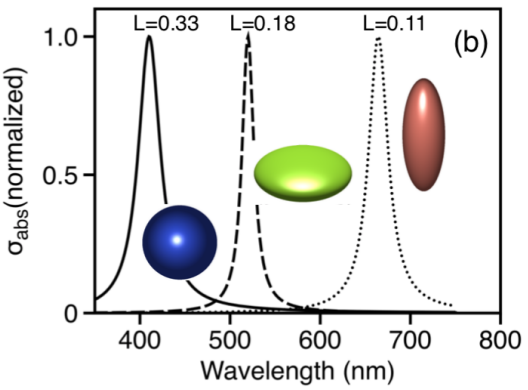

(b)

Figure 5: a) A showcase of the dependancy of shape of a plasmonic nanoparticle on the extinction spectrum and resonance wavelength, taken from [39]. b) Different shaping factors, L, and how they impact shape and resonance wavelength, taken from [28].

This thesis, however, is concerned with *bio*sensing, which entails detection of biological compounds. This is achieved through the adsorption or adhesion of said compounds onto a flat nanoplasmonic sensor while the plasmonic extinction spectrum is recorded. But before heading into the details of the ruler developed in [17], it is appropriate to conceptualize this act of sensing.

The optical spectrum measured in a plasmonic extinction experiment arises due to the fact that the light passing through the sensor interacts differently with it's components. A sensor of this type is typically composed of noble metal nanoparticles on a dielectric support, such as glass[12]. Photons of wavelengths corresponding to the resonance condition, as derived in the previous section, will interact with the plasmonic nanoparticles either by being absorbed or scattered, leading to a decrease of transmission, hence higher extinction, of light at these frequencies. A schematic illustration of this is shown in figure 6. As can be seen, an extinction peak highlighting the plasmonic resonance emerges. If, then, this sensor is subjected to a change as to the surrounding medium, a corresponding change of the peak position will be induced according to the theory detailed in the previous section. It is by tracking of this peak shift we are able to infer what is being detected. This shift of the LSPR peak, however, is dependant on *two* factors: the thickness of a potential film having been adsorbed onto the sensor, and the refractive index of the medium.

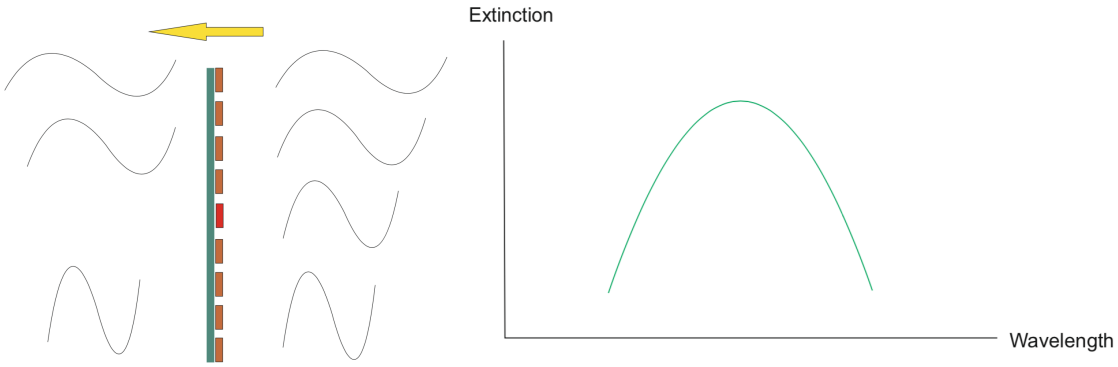

(a) (b)

Figure 6: a) A schematic depicting a plasmonic sensor comprised of homogeneous nanoparticles and the plasmon resonance induced by light of certain frequencies, with light passing from the right hand side to the left hand side, as indicated by the yellow arrow. b) An extinction spectrum with one peak, corresponding to one resonance wavelength.

The refractive index is interchangeable with the eletric permittivity, being related by

$$n = \sqrt{\mu_r} \tag{32}$$

and describes how light propagates in a medium. A film of a material forming on the plasmonic particle also attenuates the light path, and these two properties thus have the same affect on the plasmonic extinction spectrum. How to distinguish between these - deducing from which source the LSPR shift originates from - is therefore a problem when dealing with completely unknown substances.

We can thus formulate the relationship

$$\Delta R = f(t, n) \tag{33}$$

where ΔR is the shift of the plasmonic peak, t the thickness of the surrounding medium and n the refractive index. An illustration of this shift is found in figure 22

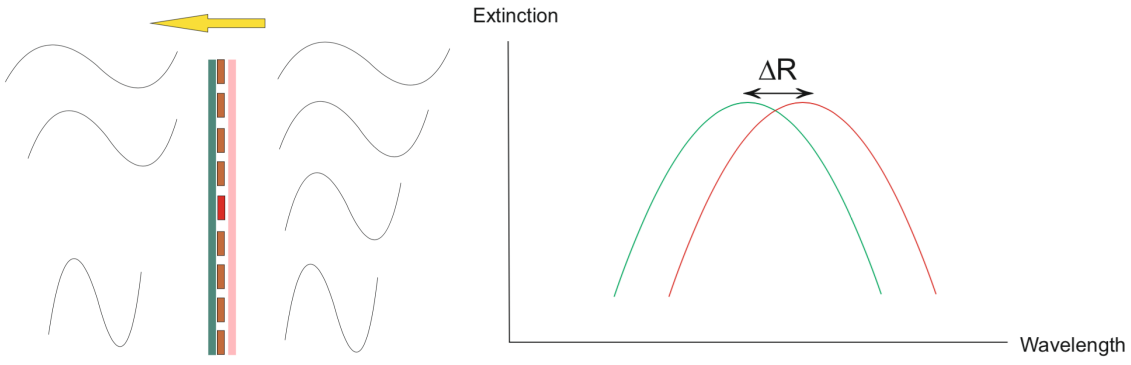

(a) (b)

Figure 7: a) A schematic depicting a film deposited on a sensor of homogeneous plasmonic nanoparticles, with light passing from the right hand side to the left hand side, as indicated by the yellow arrow. b) The shift of the extinction spectrum as a consequence of the film deposition.

As was briefly mentioned in the introduction, the most commonly used type of plasmonic sensor has been comprised of homogenous nanostructures of one material; a setup that results in one distinct peak. In [40], as a contrast, trimers of plasmonic particles interacting in complex ways gave rise to several peaks in the spectrum since different plasmonic modes where stimulated at different parts of the trimer geometry. This appearance of multiple peaks, given that they are properly separated, leads to a method of determining the system of equations represented by equation (33). Methods such as those employed in [41] and [23] utilize two sources of information in the experimental setup in order to deduce the cause of the peak shift. In [41], a quartz microbalance was used in conjunction with the plasmonic sensing. The idea is that if no mass is recorded by the QCM, the shift is induced by the different refractive index of the surrounding solution. On the other hand, any mass of an adsorbed film would be registered by the QCM, and the plasmonic peak shift was confirmed to arise due to a film having formed on the sensor. In [23], an experimental setup which utilizes the reflective property of light shone onto a sensor - where the angle of reflection is monitored rather than light extinction - is presented. The authors operate light of two different wavelengths, which results in two different plasmonic modes simultaneously being used for the sensing. What this basically entails is that two sources of information, each being affected by environmental changes differently, are built into one experimental system. The system is shown in figure 8.

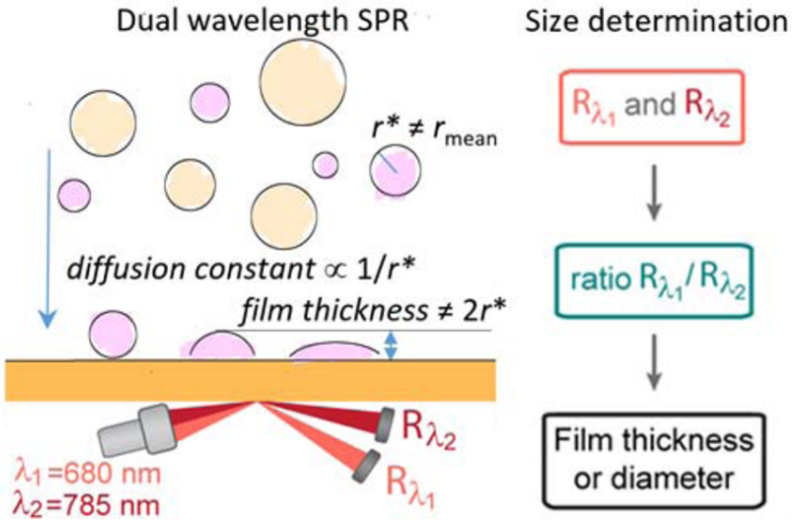

Figure 8: Schematic picture of the concept of using light of different wavelengths as well as a conceptual flowchart over the theory behind the size determination. The figure is from [23].

We are now finally in the position to present the plasmonic ruler. It is of similar composition as the topographically flat sensor outlined in [12], but instead of having noble metal nanodisks of homogeneous size, it is comprised of an ensemble of disks of two different sizes. The presence of disks of two sizes serves the same purpose as the light of two wavelengths in [23]. In this case, an extinction spectrum with two distinct peaks, each corresponding to one population of disks, emerges. The disks are all composed of silver and embedded into silicon nitride. In figure 9, a schematic of the dual-size sensor as well as an example of a spectrum produced by such a sensor is shown. The reader interested in how the sensor is fabricated and characterised is referred to [17].

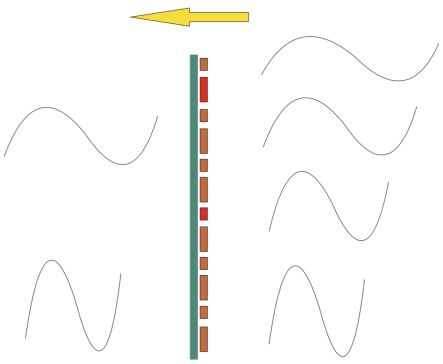

(a) The sensor.

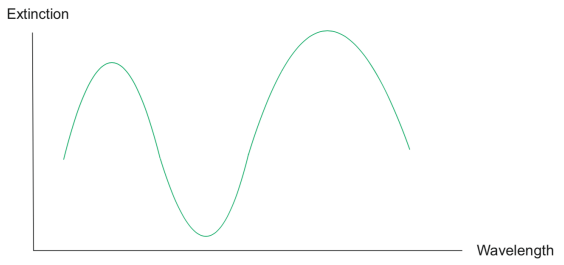

(b) Extinction spectrum showing two distinct peaks.

Figure 9: A schematic representation of the dual-size sensor and the dual peak extinction spectrum it produces, with light passing from the right hand side to the left hand side, as indicated by the yellow arrow. Larger disks correspond to resonance modes, i.e. peaks, of higher wavelengths, and smaller disks to shorter wavelengths[8].

The technique with which one deduces thickness and refractive index from the shift of the two peaks as induced by a change in the environment of the plasmonic disks follows the same procedure as that described in [23]. When a film is deposited on the sensor, the response in terms of peaks shift can be described by [31]

$$R = S(n_f - n_b)(1 - e^{\frac{-d_f}{l_d}}) \tag{34}$$

where n_f and n_b are the refractive indices of the film and the sensor, respectively, d_f the thickness of the film deposited and S and l_d parameters inherent to the sensor. S is the bulk refractive index sensitivity and is a proportionality constant regulating how large the response is given a change in the environment, and l_d is the decay length that quantifies how far the plasmonic evanescent field reaches outside the nanoparticles. The deposition of a thin film of a material onto the sensor, and the shift of the two peaks this produces, is shown in figure 10.

The sensitivity and decay length are inherent to a nanoparticle of certain chemical composition, shape and size, and thus two sets of these parameters are found in the sensor. (34) is therefore applicable for both peaks. By taking the ratio of the responses of the two peaks

$$\frac{R_1}{R_2} = \frac{S_1(1 - e^{\frac{-d_f}{l_{d1}}})}{S_2(1 - e^{\frac{-d_f}{l_{d2}}})} \tag{35}$$

where $(n_f - n_b)$ appears in both numerator and denominator and thus cancels out. The above equation, if S_1, S_2, l_{d1} and l_{d2} are known, returns d_f; the thickness of the adsorbed film. Both sensitivity and decay length can be determined through separate measurement steps, and how these are found are explained in detail in the next section.

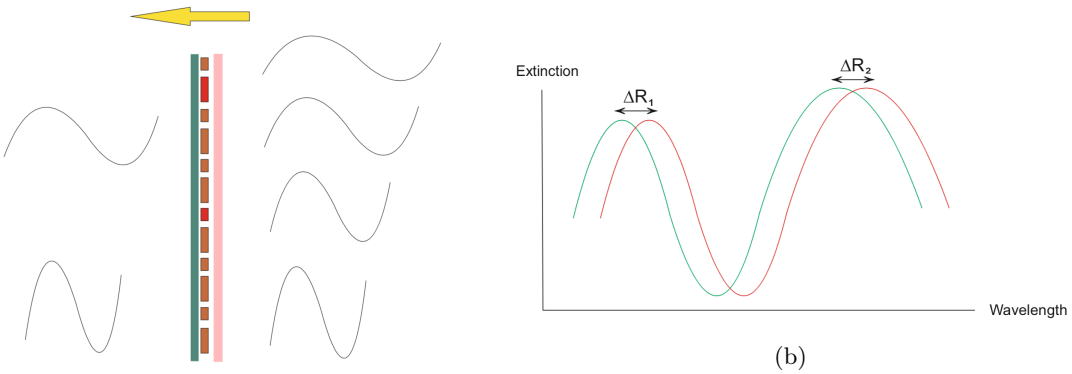

(a) (b)

Figure 10: a) Thin film deposited on the sensor. b) The shifts of the peaks as induced by the deposition of the film.

3 Experimental Methodology

In this project, two molecular systems were of main concern. The first was 1-palmitoyl-2-oleoyl-sn-glycero-3-phosphocholine (POPC), DNA and Vesicles, and the other polylysine (PLL) and silica microspheres. In this section, the experimental procedures regarding the adsorption and subsequent analysis of the thickness and refractive index of these two systems, as well as the equipment used, is presented. Furthermore, a more detailed description of the bulk refractive index sensitivity (BRIS) measurement and determination of the sensor decay length is given.

3.1 Equipment

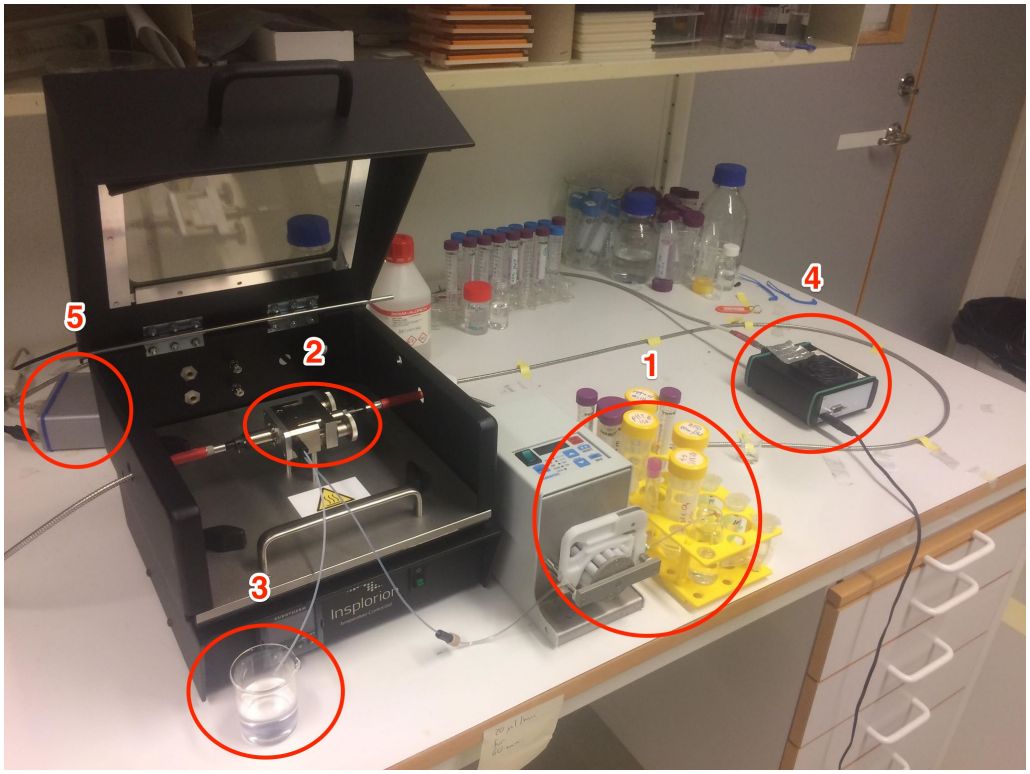

Figure 11: The experimental setup used in this project. 1) The solutions and the pump. 2) The cartridge with the sensor mounted in the XNano (the black box). 3) The outlet from the cartridge leading to the waste. 4) the lamp, connected to a power supply and 2). 5) The spectrometer, barely visible behind the Xnano, connected to 2) and the computer.

A picture of the experimental setup can be seen in figure 11. The main device used was the Insplorion XNano: the black box. Within it, a titanium cartridge through which light can be shone is mounted, and it is in this cartridge the plasmonic sensor is put. The cartridge is also connected to a thermocouple and can be heated, which enables a stable sensor temperature to be maintained. The cartridge can be seen in figure 12a. Through the cartridge is also pushed liquid, containing what molecules one wants to study, by a pump of choice. In these experiments, a peristaltic pump was used. Furthermore, the XNano was connected to both a lamp and a spectrophotometer via fiber optics. The light source used was a tungsten halogen lamp (Avantes, The Netherlands) with a maximum spectral output wavelengths of between 800 and 1200 nm. The spectrometer used was AvaSpec-2048XL (Avantes, The Netherlands). The entire setup is schematically shown in 12b.

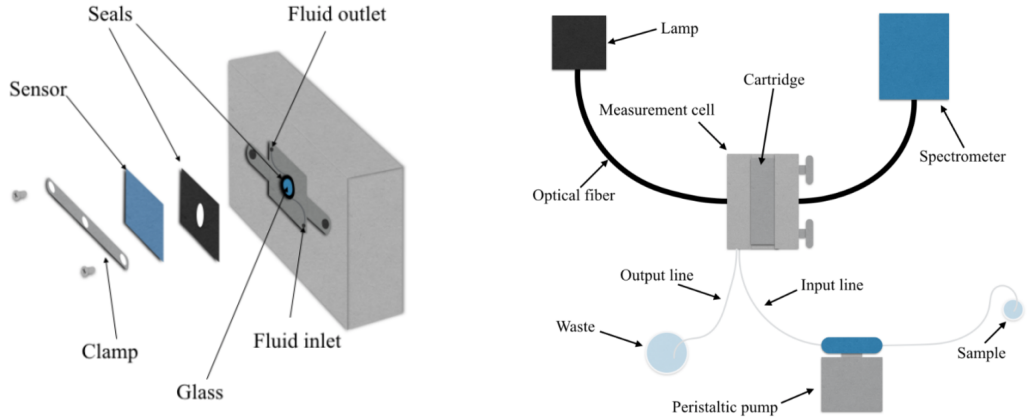

(a) (b)

Figure 12: a) A schematic image of the cartridge used in these experiments. The sensor is put on top of the seal and fastened with the clamp, and liquid is pushed by the pump through the inlet to the outlet. b) A schematic picture showing the experimental setup. The peristaltic pump pressed the liquid from the sample, through the cartridge and to the waste. Pictures taken from [17].

The spectrophotometer was connected to a computer, and it's data analysed by the Insplorer®software. The software provides a graphical interface that provides the ability to monitor peak position, peak centroid, extinction difference and extinction at the peak. Also, the spectrogram, extinction versus wavelength, as well as the peak fitting is visible. During an experiment, only one peak is fitted and thus analysed. However, the data for the full spectrum is saved and the fitting can be recalculate at one's behest, and thus both peaks are effectively tracked. The interface can be seen in figure 13.

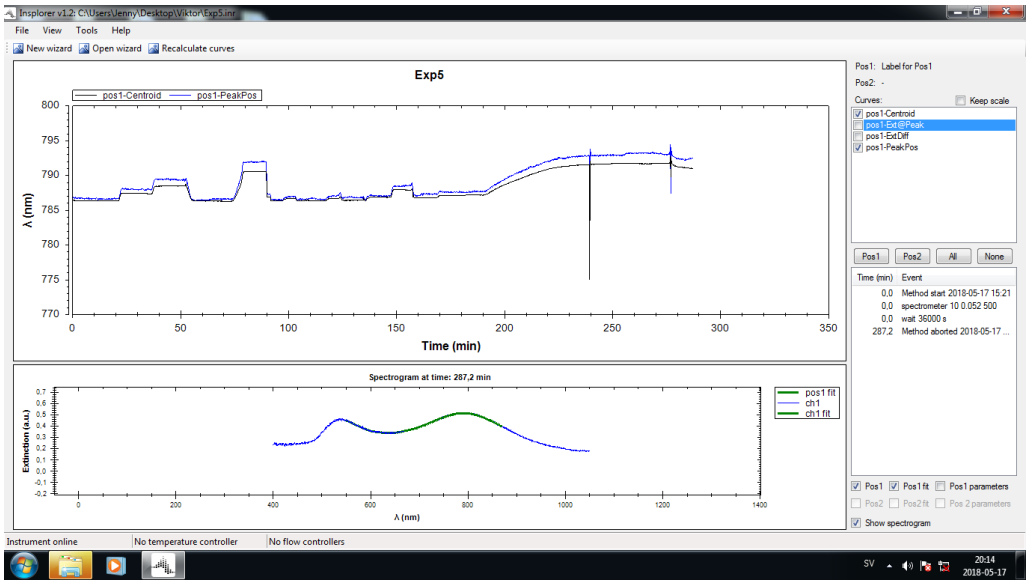

Figure 13: The interface of the software used for the data gathering. The position of the peak analysed with respect to wavelength is recorded, and both peak position and peak centroid can be viewed. At the bottom, the spectrum and how the software is fitting it can be viewed in real time.

3.2 Experimental procedures

3.2.1 Adsorption measurement of POPC, ABCD-DNA and vesicles

The sensor used was composed of Ag nanodisks of sizes 80 and 210 nm embedded in silicon nitride on a glass substrate. In order to subtract the part of the extinction spectrum originating from the glass, a glass slide with the same dimensions as the sensor was used as a reference. The glass slider was rinsed in sodium dodecyl sulfate (SDS) - an organic detergent - and Milli-Q for 10 seconds each and afterwards dried with nitrogen for 10 seconds. The sensor was immersed in SDS in an eppendorf tube and ultrasonicated for 30 minutes. The sensor was subsequently rinsed with Milli-Q for 10 seconds and dried with nitrogen for 10 seconds, after which it was treated with oxygen plasma (Harrick Plasma, USA) for 10 minutes in order for the surface to activate and ensure that the POPC bilayer adequately forms.

After the cleaning procedure, the glass slide was mounted into the cartridge and put into the XNano. The system was flushed with Milli-Q for 5 minutes to ensure some level of cleanliness as well as a stable flow throughout the system. The tubing was, prior to the experiment, flushed with SDS and Milli-Q for 20 minutes each. Afterwards, the glass slide was subjected to a buffer composed of 10 mM Bis-Tris and 150 mM NaCl, with a pH of 7.5 - a buffer composed for the purpose of keeping the biomolecules in their intended conformation. Now, a dark spectrum and a bright spectrum of the glass was taken as reference.

When the reference was taken, the pump was turned off and the glass slide removed from the cartridge and exchanged with the sensor. The flow of buffer was reintroduced, the spectrum for the sensor measured and the analysis range as well as the fitting parameters chosen. Centroid tracking was selected over peak position tracking in every experiment; this is due to centroid tracking reducing noise[42]. The buffer was flown at 50 μl/min until a stable baseline was achieved.

With a stable baseline, the buffer was interchanged with glycerol/water solutions with varying weight percent of glycerol flown at 50 μl/min. The percentage of glycerol used also varied throughout the experiments, and the exact numbers associated with each of these experiments are presented in table 1. The refractive index of pure water is 1.33303, and that of pure glycerol 1.4722. Any solution of glycerol in water would thus have a refractive index between these values, which could be determined by interpolation. The glycerol solutions were used for the bulk refractive index sensitivity(BRIS)-determination, a step that quantifies the sensors response to a change in the refractive index. The sensitivity factor, S, derived from this is expressed in nm/RIU; peak shift in nm per unit of refractive index change of the surrounding medium.

Experiment	1	2	3
Wt% glycerol	14%, 29%, 44%, 58%	10%, 20%	10.87%

Table 1: Glycerol solutions (percentage of weight) used in the POPC/DNA/Vesicle experiments.

When data for the sensitivity factor were sufficiently gathered, buffer was yet again pumped into the system, and a new baseline formed. Further species were not introduced into the system unless the baseline stabilized around approximately the same level as before the BRIS-measurements. After this, 1-palmitoyl-2-oleoyl-sn-glycero-3-phosphocholine (POPC) - lipid vesicles consisting of a closed bilayer - dissolved in the buffer with a concentration of 0.1 μg/ml were added. The POPC

was pumped at 20 μl/min. The POPC bilayer does not only facilitate further adsorption of other species, but also provides the information necessary for the determination of the decay length. This is due to both thickness and refractive index of the bilayer being known. The BRIS measurement and determination of decay length, and the subsequent determination of these parameters, is expanded on further in the data analysis subsection.

When the POPC bilayer was adequately formed - the condition for this is explained later - the pumped solution was yet again switched to buffer. The pump speed was from this point maintained at 20 μl/min. If the signal during this session of buffer was steady, the conclusion that the POPC bilayer was stable could be drawn, and 500 nM ABCD-DNA, which by virtue of it's cholesteryl group anchors to the POPC bilayer, was added. The same procedure as with the POPC was followed, and a when a stable signal during flow of buffer was present, spherical vesicles (1 mg/ml) - which in turn had a group complementary to the ABCD-DNA, and thus attaches to it - was flown through the cell, and the plasmonic response recorded. Buffer was yet again reintroduced, and if the signal was stable, the whole compound of POPC, DNA and vesicles was deemed stable, and the measurement finished. The final compound is shown in figure 14.

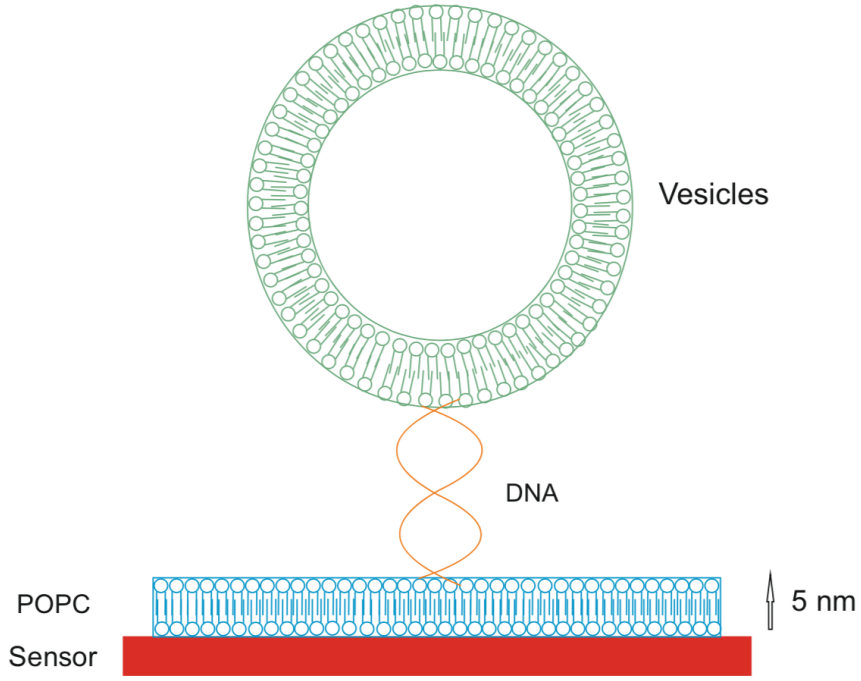

Figure 14: A schematic picture of the final compound produced in the experiment, with a POPC bilayer of known thickness (5 nm) formed on top of the sensor, DNA anchored to it and a spherical vesicles bound to the DNA.

3.2.2 Adsorption measurements of PLL and Silica Nanoparticles

The same sensor as described in the previous subsection was used in these experiments. The preparations were similar, with the only difference being that the sensor was processed in UV and ozon (ProCleaner, BioForce Nanosciences, USA) for 30 minutes in order to both clean the surface from organic compounds, but also to activate it.

After the cleaning procedure, the glass slide was mounted into the cartridge and put into the

XNano. The system was flushed with Milli-Q for 5 minutes, and the tubing was, prior to the experiment, flushed with SDS and Milli-Q for 20 minutes each. Afterwards, the glass slide was subjected to a buffer composed of 10 mM Bis-Tris and 150 mM NaCl, with a pH of 7.5.

The reference was then taken according to the same procedure as described in the previous subsection. With a stable baseline, the buffer was interchanged with glycerol/water solutions with varying weight percent of glycerol. The glycerol solutions used in these experiments are shown in table 2. After the data for the sensitivity determination was gathered, buffer was reintroduced. When a new baseline had formed, Polylysine (PLL) - a polypeptide - was introduced. The PLL, after having electrostatically attached to the surface of the sensor, was subjected to buffer in order to confirm that the layer was stable. If it was, a solution of silica nanoparticles (Polysciences Inc, PA, USA) with a concentration of 5 μl/ml buffer was added. The Si NPs were 50 nm in diameter. The PLL and Si NPs interact electrostatically, and maintained stability during flow of buffer. The final molecular compound is visualized schematically in figure 15.

Due to the inability to determine decay length, POPC was added in accordance with the procedure presented in the previous subsection during one of the experiments.

Experiment	4	5
Wt% glycerol	5.435%, 10.87%, 14%	5.435%

Table 2: glycerol solutions (percentage of weight) used in the silica experiments.

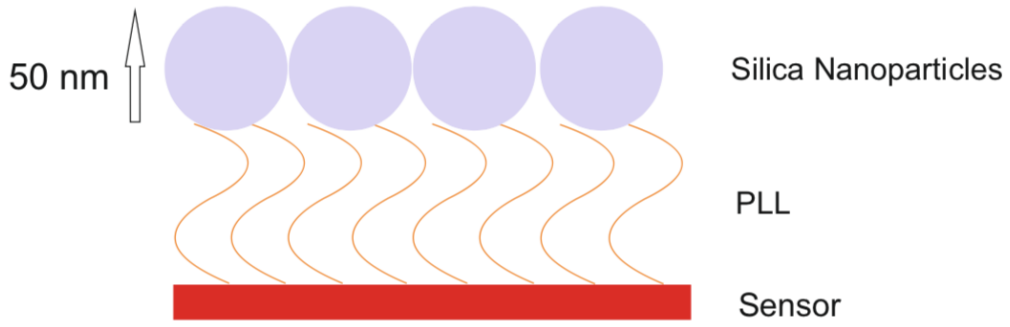

Figure 15: A schematic picture for the final compound in the PLL/Si NPs experiment, with PLL bonded to the sensor and silica nanoparticles(50 nm).

3.2.3 Data analysis

The two main steps needed before a complete set of data, that is thickness as a function of time, could be produced was BRIS and decay length. The BRIS measurement was achieved through the steps of glycerol at the beginning of the experiment, where the shift of the peak position as induced by the change in refractive index around the sensor is recorded. The values of shift with corresponding change in refractive index are plotted on a line, and regression analysis is employed in order to calculate the slope of the line. The sensitivity factor, S, is this slope - assuming that the refractive index as a function of concentration and wavelength of the incoming light is linear. An example of the BRIS measurement as well as the linear regression can be seen in figure 16.

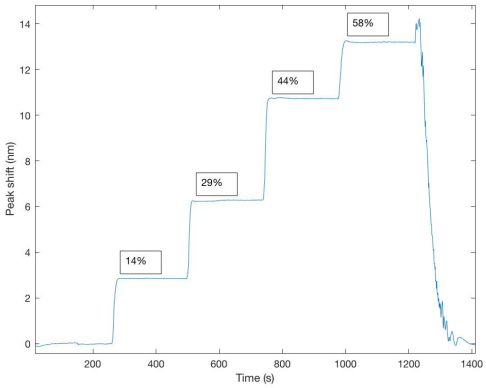

(a)

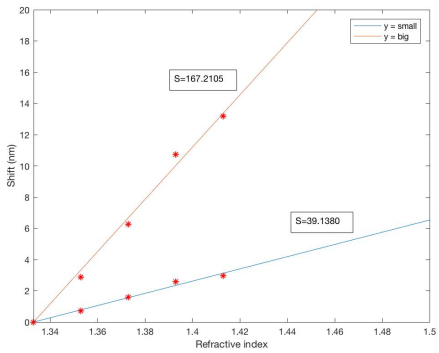

(b)

Figure 16: a) The steps of peak shifts with increasing concentration of glycerol (concentration can be seen in the textboxes above each plateau). b) The linear regression of peak shift as a function of refractive index. The S factor for the small disks in this example is 39.1380 nm/RIU, and the big disks is 167.2105 nm/RIU.

The decay length, in turn, is determined through the use of equation (34). If rewritten

$$l_d = \frac{-d_f}{ln(1 - \frac{R}{S(n_f - n_b)})} \tag{36}$$

the decay length, l_d is readily determined given that d_f, the thickness of the adsorbed film, R, the peak shift induced by the adsorption, S, the sensitivity factor, and n_f and n_b, the refractive indices of the film and the bulk(water) respectively, are known. This is what the usage of POPC aims to deliver. The thickness of the POPC bilayer has been determined as 5 nm[43], and the refractive index as 1.48[44], and with these values, together with the already determined sensitivity, l_d can calculated. Figure 17 displays the response of the adsorption and subsequent formation of the POPC bilayer.

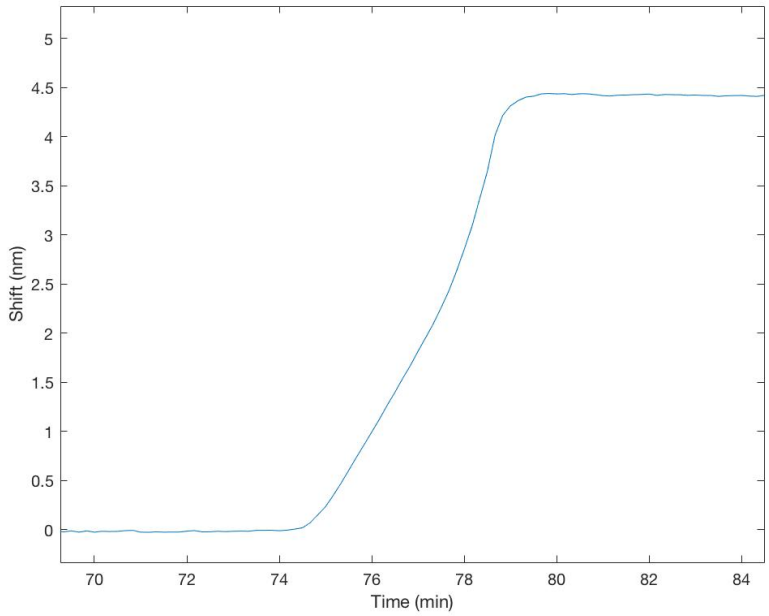

Figure 17: The peak shift induced by the adsorption and subsequent formation of the POPC bilayer.

The two parameters, S and l_d, is determined by the above mentioned means for both the small and big disks of the plasmonic ruler. Hence, equation (35) is fully determined with respect d_f; the thickness of the adsorbed film. The right hand side of (35) can thus be plotted as a function of thickness - a plot that in this report is called the masterplot - as that showcased in figure 18.

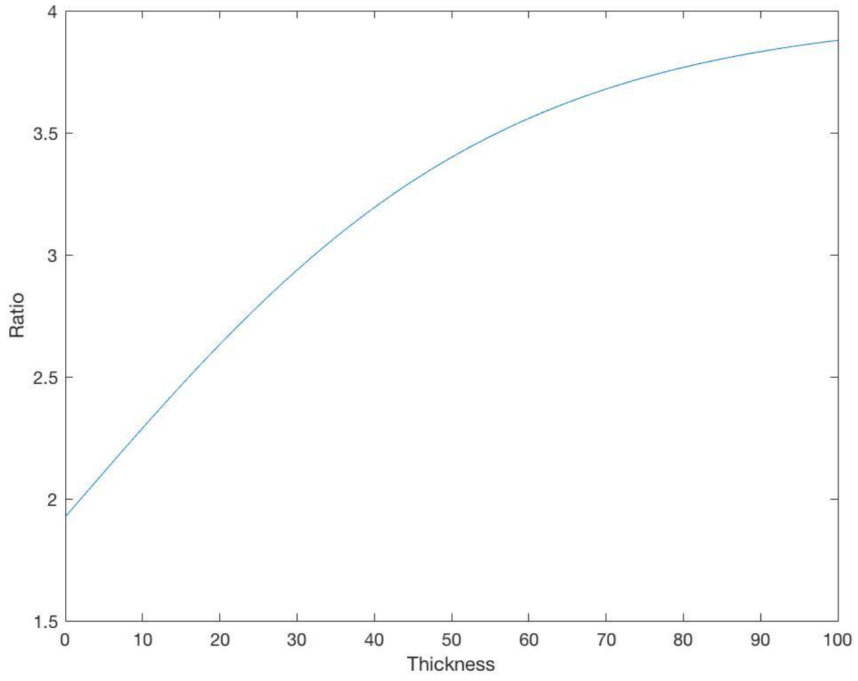

Figure 18: A plot over the ratio of peak shifts as a function of thickness (nm). Plot made from the parameter values calculated from figure 16.

The data of the peak shifts for the two disk sizes as a function of time are therefore divided with each other, and a plot of the ratio, the left hand side of (35), as a function of time is produced. This plot is then converted, through the masterplot, into a graph of the thickness evolution in time of the system studied. With the thickness of the different adsorbed species known, their refractive indices could be calculated through a rearrangement of equation (35)

$$n_f = \frac{R}{S(1 - e^{\frac{-d_f}{l_d}})} + n_b \tag{37}$$

4 Results and Discussion

First and foremost; the initial phase of this thesis was the establishment of an experimental setup in which the signal to noise ratio was improved. The parameters that can be varied in order to achieve this are quite limited; temperature and flow rates during the experiments have to be held at values that assure the stability of the biological compounds used. What can more easily be adjusted, however, is the equipment used. Figures 19, 20 and 21 show simple extinction spectrum measurements with glycerol on the same sensor as in the other experiments. The data is from three different spectrometers: AvaSpec 1024, AvaSpec 2048XL, and AvaSpec 3648. Above each plateau in the three figures is the standard deviation belonging to it. Even though the measurements for the three spectrometers were run for different amounts of time, this analysis is a qualitative one and it is obvious that the AvaSpec 2048XL, figure 20, has the best signal-to-noise ratio, and it was therefore used in every experiment.

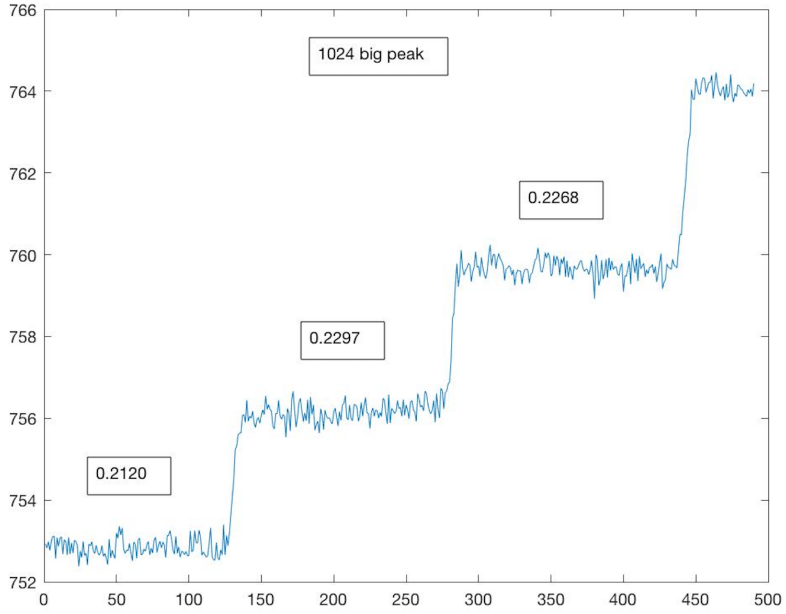

Figure 19: The spectrum obtained using steps of glycerol with AvaSpec 1024, the standard deviations of the errors visible above each plateau.

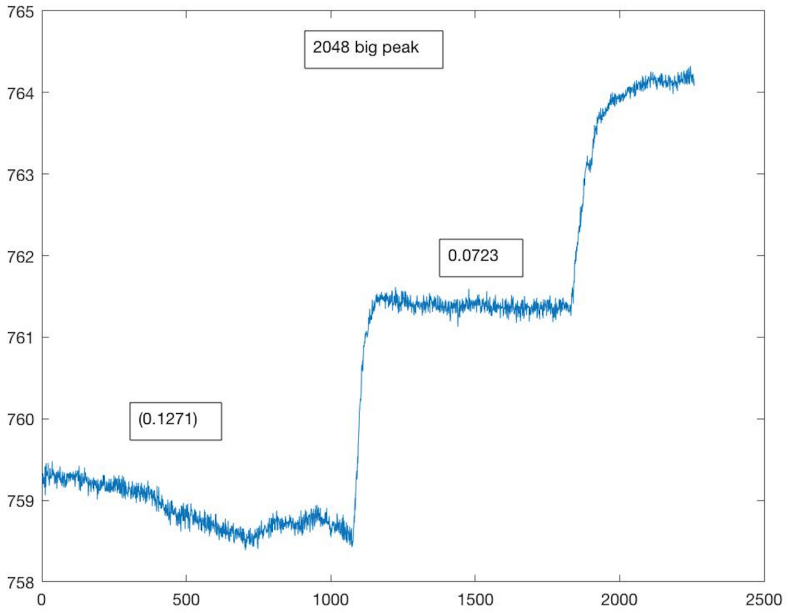

Figure 20: The spectrum obtained using steps of glycerol with AvaSpec 2048XL, the standard deviations of the errors visible above each plateau.

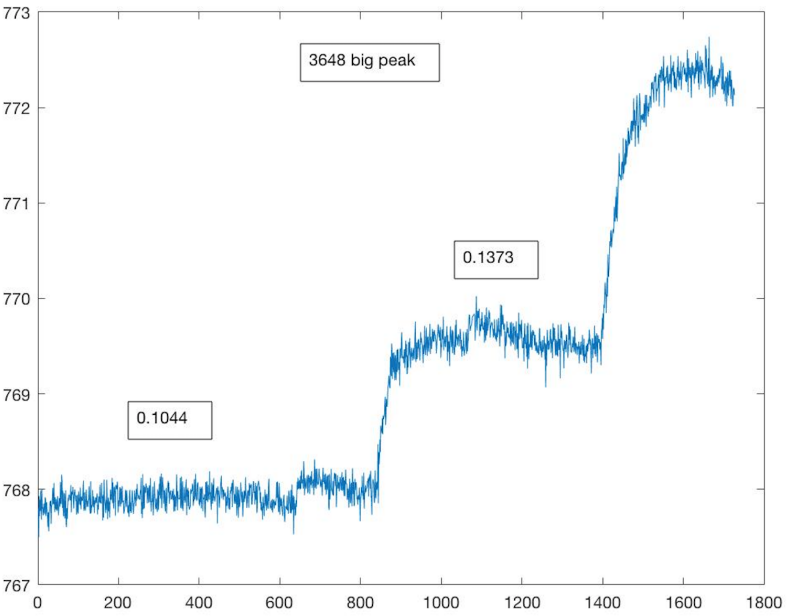

Figure 21: The spectrum obtained using steps of glycerol with AvaSpec 3648, the standard deviations of the errors visible above each plateau.

4.1 Adsorption measurements

4.1.1 Experiment 1 (POPC/DNA/Vesicle)

We begin by presenting the experimental data obtained from the first full measurement of the POPC/DNA-system. The peak centroid tracking can be seen in figure **??**. At around 10 minutes, the BRIS measurement commenced, and a more detailed depiction of this can be seen in figure 23.

At 65 minutes, POPC was added to the system, and DNA was subsequently added at 110 minutes. Finally, the spherical vesicles were added at 179 minutes. The sensitivity factor was determined to be 39.1380 nm/RIU for the small peak and 167.2105 nm/RIU for the big peak, as seen in figure 24

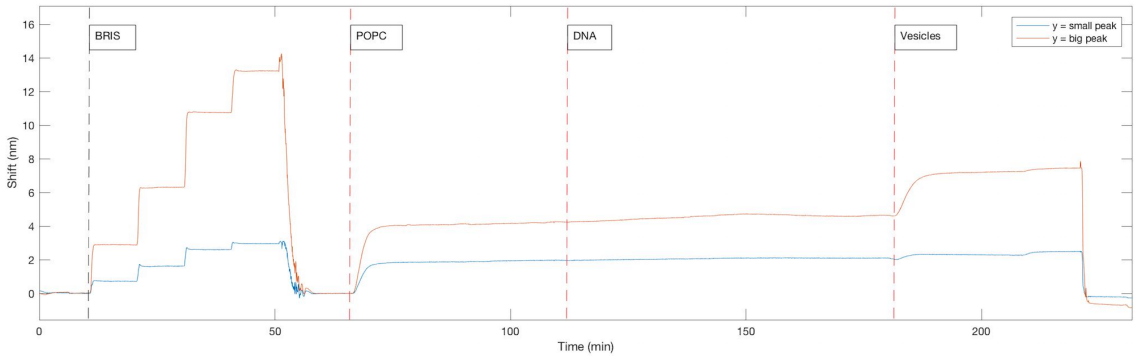

Figure 22: The centroid tracking from the first experiment. The shift from the reference position in nm as a function of time is displayed. The major features of the graph are marked by dashed lines and a note detailing the measurement made or the species used at that time.

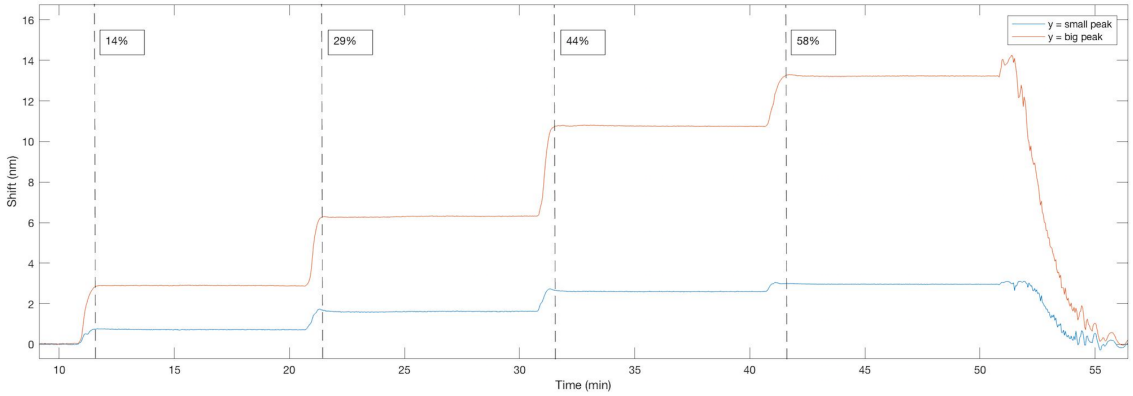

Figure 23: The steps of peak shifts with increasing concentration of glycerol, with the weight percentage used shown at each step.

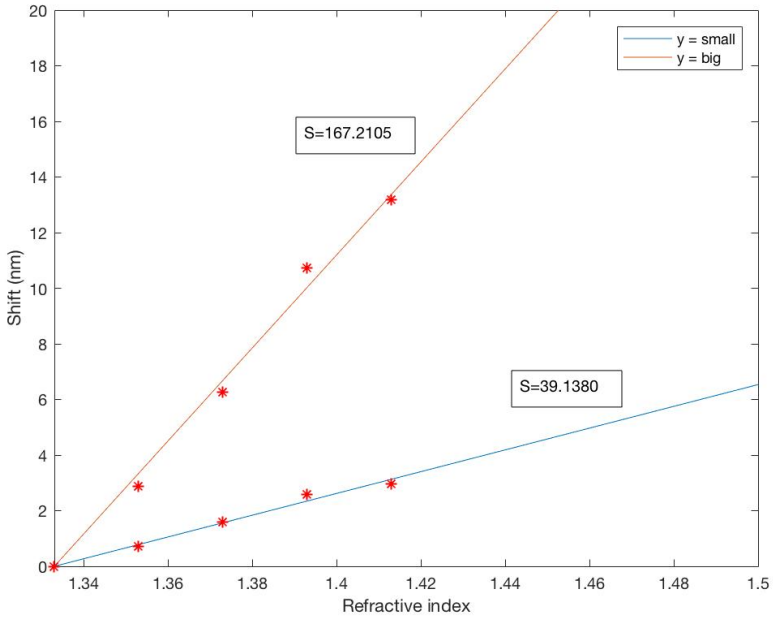

Figure 24: The BRIS measurement from the first experiment displaying the sensitivities, in nm/RIU, for both the small and big peak.

The decay length, however, could not be determined. For this to be possible, the POPC vesicles had to rupture and adequately form the bilayer of which the thickness and refractive index is known, and this did not happen. In other words, equation (38) was not applicable. The POPC addition as registered by both the big and small peak in the first experiment can be seen in figure 25a, and figure 25b displays the comparison with a successful formation of the POPC bilayer. It is the characteristic kink being visible in the middle of the slope, as well as the sharp saturation, that distinguishes a successful POPC bilayer formation[45]. The kink separates two regions of different slope, and the sharper slope after the kink represent an acceleration of increased thickness. This is due to the reaching of a critical POPC concentration on the surface at which adjacent vesicles rupture and bind to each other, forming a continuous bilayer[46].

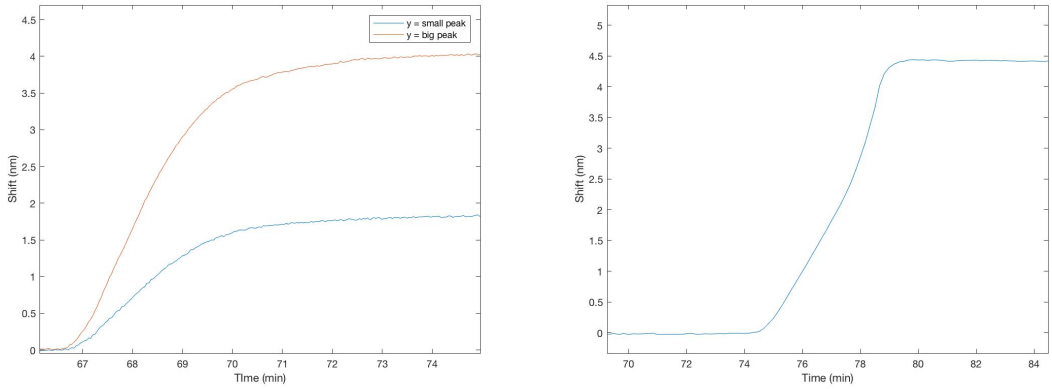

(a) (b)

Figure 25: a) Unsuccessful formation of the POPC bilayer. b) Example of a successful formation of the POPC bilayer, recognized by the characteristic kink separating two regions of different slope in the graph, as well as the sharper saturation of the signal.

With the conclusion that the POPC bilayer did not adequately form, further analysis of the data - i.e. a rendition of the thickness evolution of the system - is redundant. We therefore move on to the second experiment.

4.1.2 Experiment 2 (POPC/DNA/Vesicle with surface activation of the sensor)

In order to remedy the unsatisfactory bilayer formation, the sensor was prior to the second experiment treated with oxygen plasma[47], as explained in the Experimental Methodology section. The results - peak centroid shifts, ratio of the centroid shifts and thickness evolution - are presented in figure 26, figure 27 and figure 28, respectively.

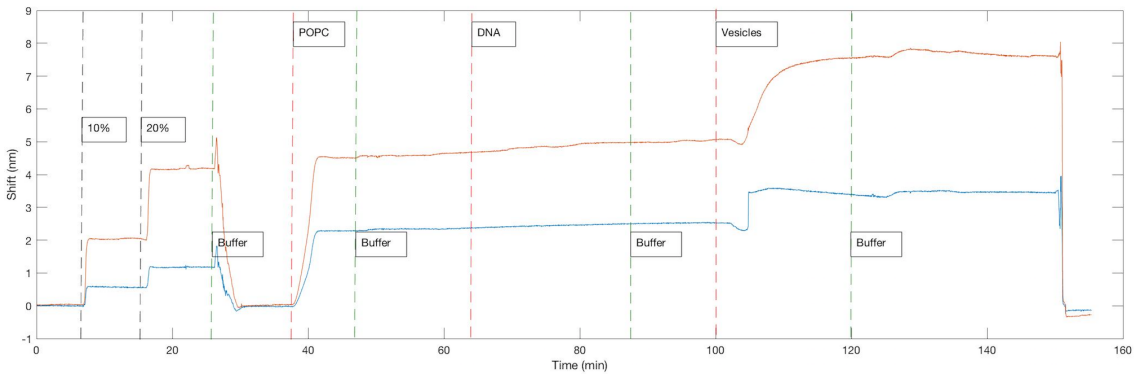

Figure 26: The centroid shifts of the big and small peak from the second experiment, with key features marked.

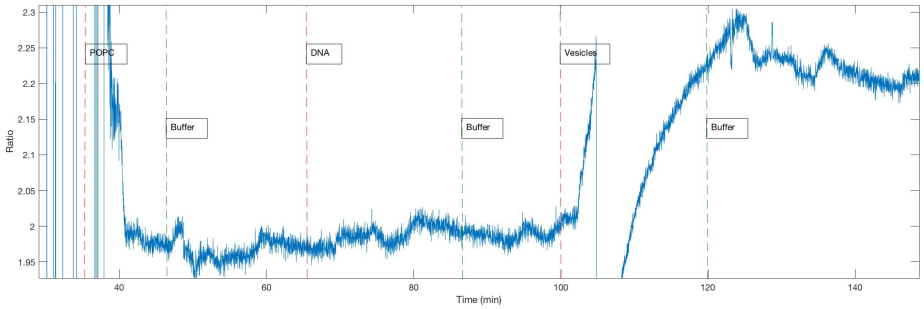

Figure 27: The ratio of the centroid shifts of the big and small peak, with key features marked.

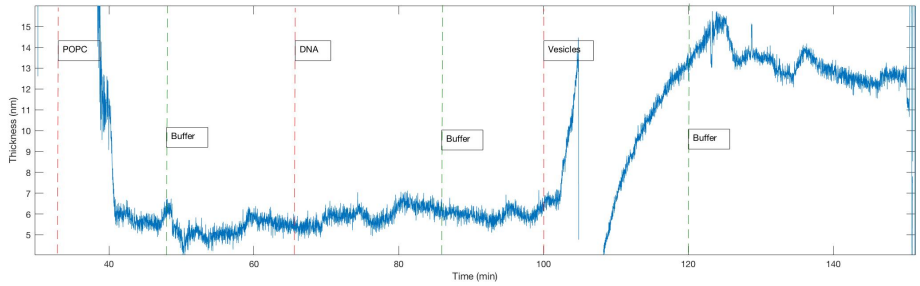

Figure 28: The thickness evolution of the system, with key features marked.

As can be seen in figure 29, the shift of both peaks indicates that the POPC bilayer adequately formed, and thus the decay length could be determined as 12.9 nm for the small peak, and 25.5 nm for the big peak.

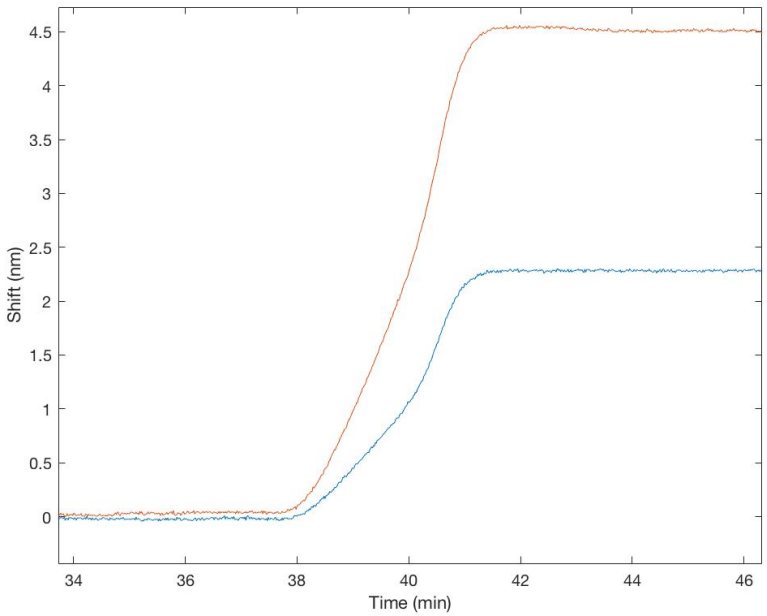

Figure 29: Successful formation of the POPC bilayer.

The BRIS measurement from the second experiment can be seen in figure 30, and the sensitivities

were determined as 47.8547 nm/RIU for the small peak, and 168.9186 nm/RIU for the big peak.

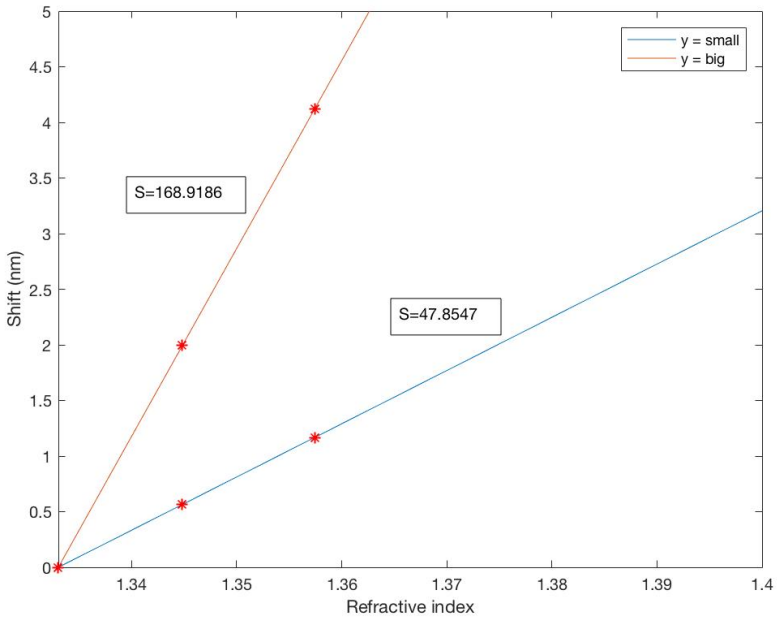

Figure 30: The BRIS measurement from the second experiment displaying the sensitivities for both the small and big peak.

Some interesting things can be noted in the data from the second experiment. Looking at figure 26, a qualitative difference between the responses of the two peaks after the addition of vesicles can be noted. Firstly, the small peak saturates both faster and earlier, and secondly, the signal decreases for the small peak whereas it increases and subsequently saturates for the big peak. This is the cause for the strange behaviour of the ratio and thickness between 100 and 110 minutes. Naturally, the decrease of the signal from the small peak affects the ratio, and thus the thickness, and is the source of the increased thickness even after the vesicle solution was changed to buffer. Even so, both signals flattens out after 140 minutes, and we therefore treat this as the final thickness of the whole compund. Looking at figure 28, POPC averages around 5 nm in thickness, which is given since it is this value that is used as calibration through the calculation of the decay length. The thickness of the DNA, on the other hand, is hard to distinguish. Only a tiny increase of the average between the region with only POPC and the one with DNA on POPC can be seen, and this is still with a rather large error. The only real proof that the DNA attached to the POPC is the fact that the vesicles subsequently attached to the DNA, and were stable even after addition of buffer around 120 minutes. The thickness of the DNA, which is of unknown length, can not be accurately confirmed by this measurement. The spherical vesicles attaching to the DNA was 65 nm in diameter, which is far larger the 8 nm obtained from the measurement. The reason for this is hard to determine; it can either by due to an inherent problem in the measurement procedure - such as the sensitivity or the decay length not being adequately determined - a structural problem of the molecular system studied, or anything in between. The sensitivities are derived, as stated multiple times, from how the nanoplasmonic extinction spectrum reacts to changes in the refractive index of the immediate environment of the particles comprising the sensor, and is thus dependant on other species, i.e. contaminants, being present. However, if these hypohetical contaminations are static, the error should be propagated throughout the calculations and cancelled, i.e. they become a part of the background reference. A departure from this case, however, may be present if

the contaminations were to be removed during the measurement. In order to make sure this does not happen, a thorough and systematic cleaning procedure of the sensor prior to the experiment is necessary.

However, one should note that the vesicles are indeed hollow and filled with water, and if it is assumed that the thickness of the lipid bilayer is similar to that in POPC, 5 nm, the results from the second experiment suddenly seem much more valid. In this case, the final thickness that can be sensed within the decay length should be a bit over 10 nm (POPC + vesicles), where the uncertainty comes from the DNA. A further remark is that the decay length for the small peak was in this experiment determined as 12.9 nm and the big as 25.5 - a vesicle of 65 nm would lie outside of both of these ranges. Considering this lends further credibility to the accuracy of the thickness determination for the whole compound.

Furthermore, on a more general note; a possible structural explanation for unaccurate thickness determination is as follows: the DNA, being an oblong molecule, can be directed in a variety of directions when anchored to the POPC. Thus, the registered thickness could, approximately, be between the width and the length of the DNA molecule. The exact dynamics of DNA molecules on a POPC surface has to be known in order to make a thorough analysis of the possible situations, but let us visualize that few DNA molecules attach to the POPC, i.e. the surface density of DNA on the POPC surface is small. Moreover, if the DNA lies down due to interactions with the surface, the vesicles may have difficulties bonding to it. The thickness registered would thus be vesicles moving in close proximity to the sensor disks. Another possible explanation for the low thickness is that the spherical vesicles actually were smaller than 50 nm in diameter, and the reason for this may either be that the extrusion was unsuccessful, or that the batch was old enough for the vesicles to restructure themselves and thus form a polydispersed solution.

Another source for the inaccurate data may be fact that the sensitivity could change throughout the experiment. The sensitivity is indeed dependant upon how and in what the sensor is embedded, and how far from the sensor the object registered is. However, if it is the case that sensitivity changes with additional adsorbed species, then surely the decay length changes as well. Therefore, in order to obtain more accurate data, a method through which both sensitivity and decay length can be corrected throughout an experiment has to be found. An attempt at this is presented by the third experiment.

4.1.3 Experiment 3 (POPC/DNA/Vesicle with repeated glycerol steps)

The shift plots for the third experiment can be seen in figure 31. One immediately notice a distinct departure in the data compared to the previous experiment; around 190 minutes, the signal begins to fluctuate and suddenly drop a substantial bit. This was concluded being the cause of a bubble forming inside the measurement chamber, moreover a bubble that was large enough so that it was impossible to remove it by extensive flushing.

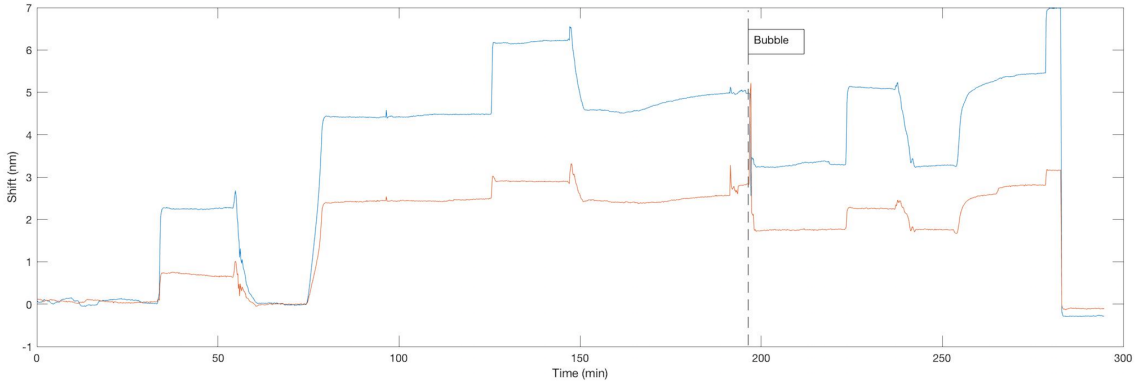

Figure 31: The shift plots from experiment three, displaying the sudden drop in signal due to the bubble.

Even though the bubble seemingly ruined the measurements, the data was adjusted in order to salvage what knowledge could be gathered. The spectrum was removed around the creation of the bubble and lifted at 200 minutes to match the signal level before the bubble. The shift spectrum can be seen in figure 32, and the thickness in figure 33. During this experiment, only one solution of glycerol was used (10.87%), and the sensitivities were determined as 43.5926 nm/RIU for the small peak and 141.7687 nm/RIU for the big peak. The decay length was 10.6354 nm for the small peak and 21.1378 nm for the big peak.

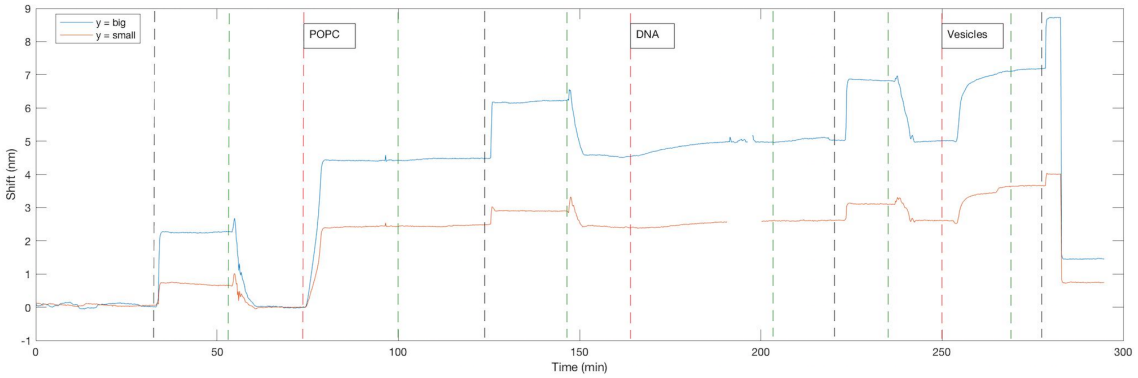

Figure 32: The shift plots from experiment three with correction for the bubble. Red lines are explained by the textboxes attached to them, green line represents buffer and black glycerol. The glycerol concentration used in this measurement was 10.87%.

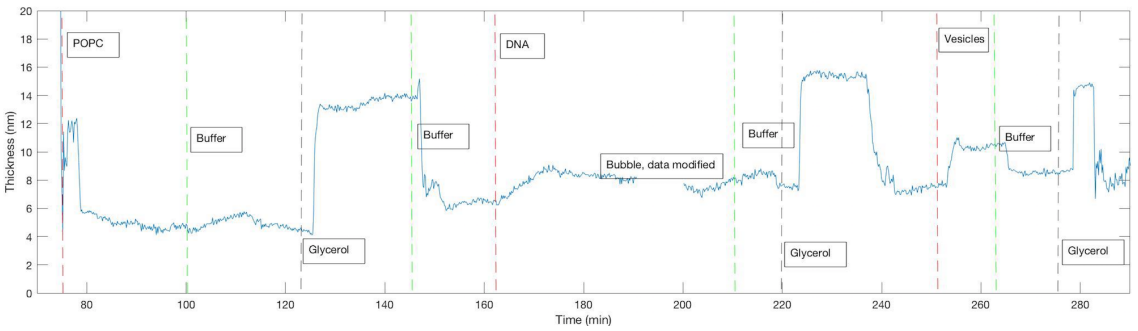

Figure 33: The thickness from the third experiment.

Looking at figure 32 and figure 33, we can see that there is a difference in signal for the first two glycerol plateaus: the one right after the buffer baseline, and the one after POPC is deposited. A calculation of the BRIS from the second plateau gives 28.0146 nm/RIU for the small peak and 107.8972 nm/RIU for the big peak. Even though, as mentioned above, the decay length also need to be redetermined in order for the analysis to be correct, the thickness was recalculated using the new values for the sensitivity. New decay lengths were calculated using these sensitivities, while the response part of equation (38) stemming from the POPC adsorption remained the same. The thickness is shown in figure 34, were only the main steps are highlighted for the quantitative comparison with figure 33.

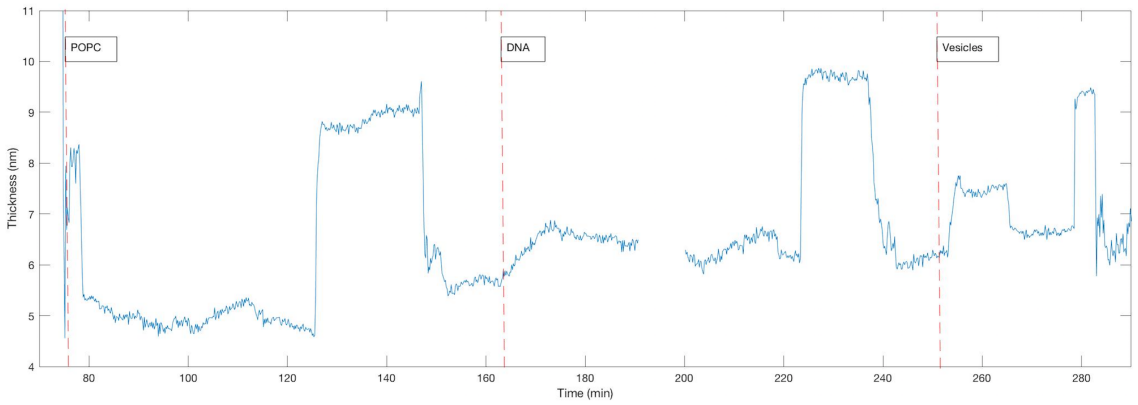

Figure 34: The thickness from the third experiment recalculated using BRIS from the second peak (after POPC deposition).

In 33, the thickness of the whole compound after addition of DNA lies just over 8 nm, while in 34 it is around 6.5 nm. This demonstrates that the results can differ substantially with changing sensitivity. A total thickness of 8 nm gives a value of 3 nm for the DNA, which is around the same value that the data from the second experiment hints at.

Another problem one can detect in figure 33 is that the baseline after the second glycerol step, after adsorption of POPC, is not reverted to the same level as before the glycerol. This problem may be remedied by simply letting the buffer flow for a longer amount of time. Even so, it is not that surprising that glycerol, when interacting with POPC - a lipid membrane - leaves a permanent mark on the signal, since glycerol itself is a component of a lipid membrane and thus have a high solubility in it[48]. It may thus be a good idea not to add glycerol, i.e. do a BRIS measurement, after addition of POPC. Moreover, if one only observes the shift induced by DNA from this higher level, the thickness is rather around 1.5 nm than 3, and this is even more close to the result from the second experiment.

Furthermore; the vesicles used in this experiment were smaller (35 nm) than before (65 nm) in order to circumvent any potential problem with the detection range of the sensor being too small. Still, the thickness of the vesicles can in this experiment not be derived. Looking at 33, the signal is not stable when vesicles are exchanged with buffer, i.e. the buffer flushes away the vesicles, and thus, they do not adequately bind to the DNA. This problem may solely be due to an inability of the vesicles to reach the surface, due to the bubble.

A positive development worth pointing out between the second and third experiment is a decrease of the error. A comparison of the errors at the adsorption of DNA is seen in figure 35. 35a displays the second experiment with a standard deviation of 0.3572, and 35b the third experiment with a

standard deviation of 0.2443. It can further be noted that in 35a, the signal fluctuates in a range of 1 nm, while in 35b, the range is rather 0.5 nm. The source for this increase in accuracy is the settings of the signal processing during the measurement; in the second experiment, the data collection frequency was 1 HZ and in the third 0.1 HZ. This longer time between readings produces a more smooth spectrum.

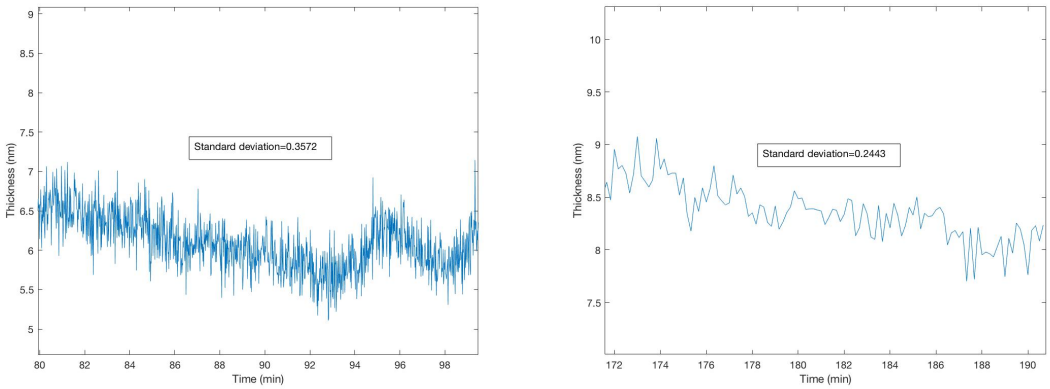

(a) (b)

Figure 35: The error during DNA adsorption for a) the second experiment and b) the third experiment.

4.1.4 Experiment 4 (PLL/Si NPs)

Considering the relatively unsatisfying results from three experiments on the POPC/DNA/vesicle system, another, more simple, molecular system was studied. This was silica nanoparticles (Si NPs) on polylysine (PLL) and the BRIS plot is shown in figure 36, the shift plots are shown in figure 37 and the thickness in figure 38.

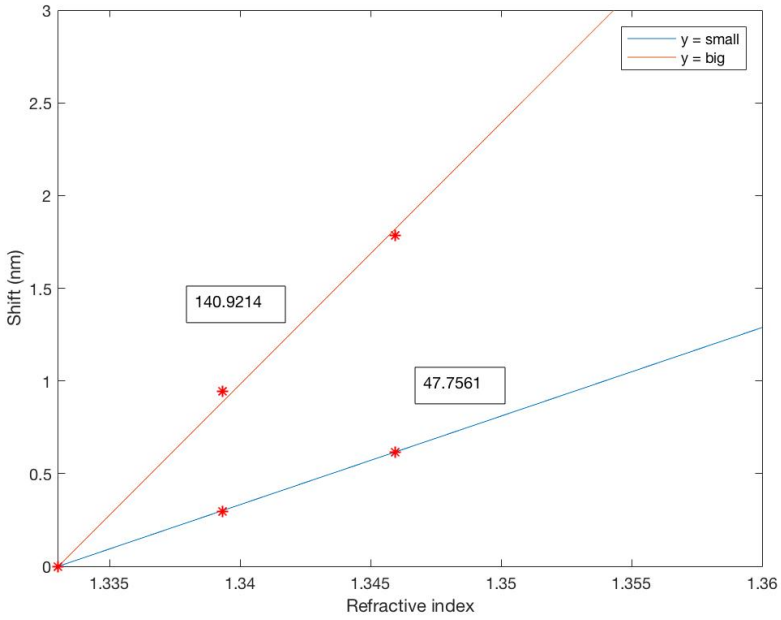

Figure 36: The BRIS plots from experiment 4, the sensitivity was determined as 47.7561 nm/RIU for the small peak and 140.9214 nm/RIU for the big peak.

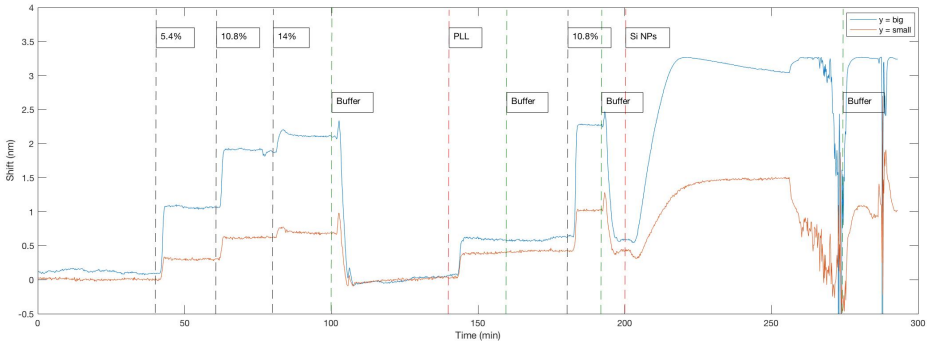

Figure 37: The shift plots from experiment 4.

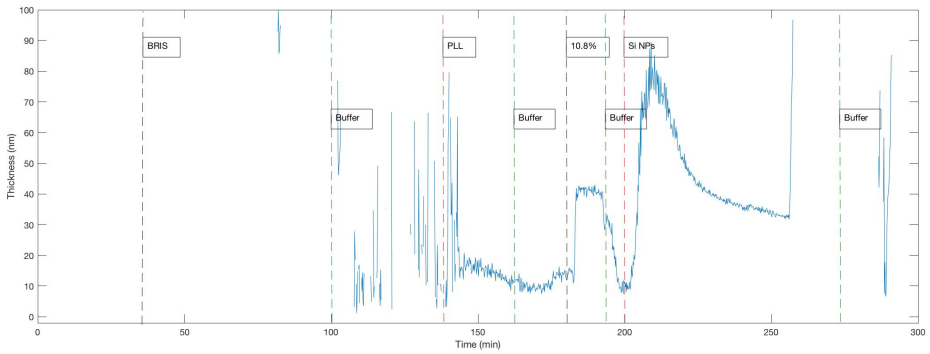

Figure 38: The thickness from experiment 4.

The sensitivites were determined as 47.7561 nm/RIU for the small peak and 140.9214 nm/RIU for the big peak, but a decay length was not determined in this experiment. The reason for the lack of decay length is that no lipid bilayer of known length, such as POPC, or the like was used during the measurement. Figure 37 and figure 38 are thus created using the decay lengths from the previous experiment. As can be seen in 38, the PLL layer averages about 10 nm in thickness, and apart from the previous experiment, glycerol does not seem to leave any permanent mark on the signal, since the same level is reached after the glycerol step at around 190 minutes. The Si NPs, on the other hand, behave rather strange. If one looks at figure 37, the signal from the small peak flattens out and stabilizes at the same time as the signal from the big peak starts to drop. The drop continuous until a sudden spike back to the saturation level. The small peak, however, almost completely loses it's signal at this time, and never regains the same saturation level. This behaviour is indeed stranger than that of the POPC/DNA/Vesicles system, were such spikes in signal were not present. When buffer is reintroduced at around 275 minutes, the signal for the big peak is stable at the saturation level, which at least indicates that the PLL/Si NP electrostatic interaction is strong. A further testimony to this is that the signal was really hard to decrease even when the system later was flushed with SDS and Milli-Q. If we focus on the part immediately after saturation, the thickness is around 70 nm, even though the noise is quite large. Subtracting the 10 nm stemming from the PLL, this leaves a thickness of 60 nm for the Si NPs, which interestingly enough is close to the true diameter of 50 nm[49].

4.1.5 Experiment 5 (PLL/Si NPs with POPC deposition)

We now move on to experiment number five, which was also conducted with PLL and Si NPs. The shift plots are shown in figure 39

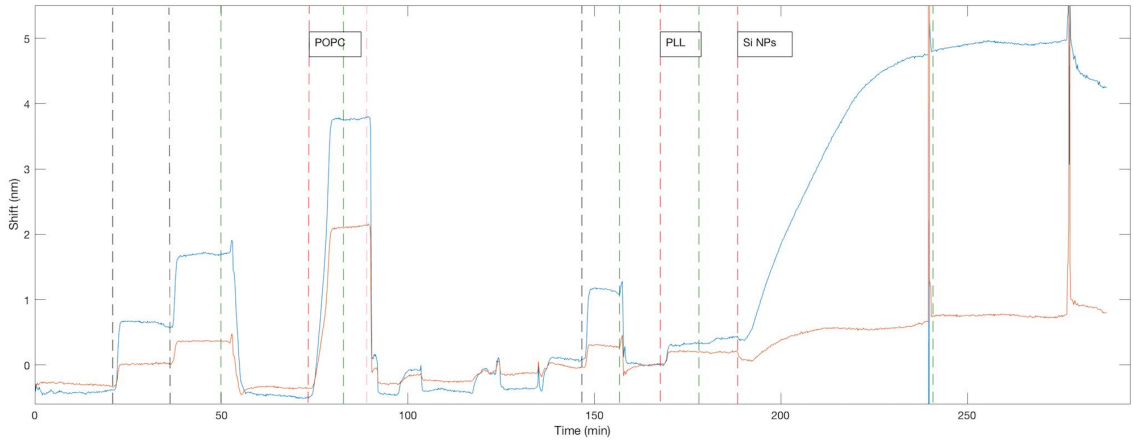

Figure 39: The shift plots from experiment five, displaying the main features with red lines and text boxes. Black lines are glycerol(5.43% and 10.87%), green buffer and pink SDS.

A BRIS measurement was conducted at the beginning using glycerol solutions of concentrations 5.43% and 10.87%. After this, a POPC adsorption step was made in order for the decay length to be determined. The POPC rupturing can be seen in figure 40, which proves that the decay length could satisfyingly be determined. The sensitivites were determined to 51.00 nm/RIU for the small peak and 166.16 nm/RIU for the big peak, and are displayed in figure 41. The decay lengths were 15.1224 nm for the small peak and 29.8749 nm for the big peak.

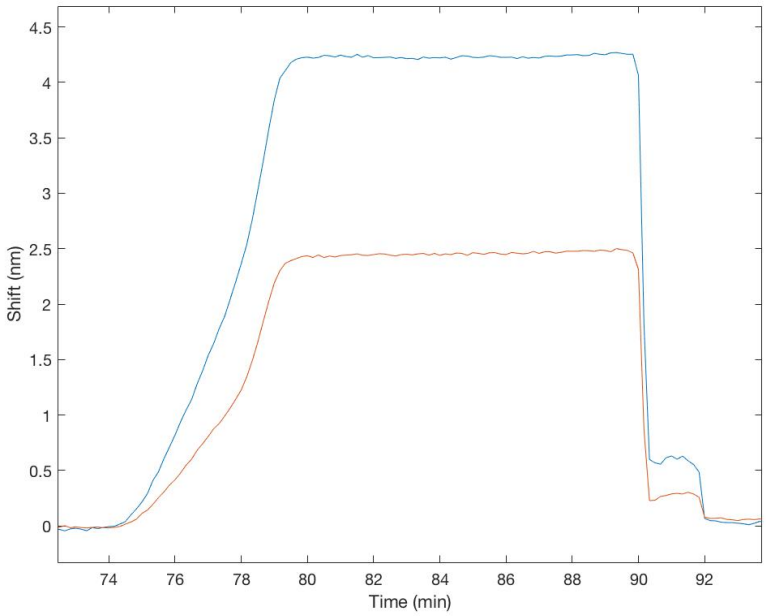

Figure 40: The successful rupturing and subsequent bilayer formation of POPC from experiment 5.

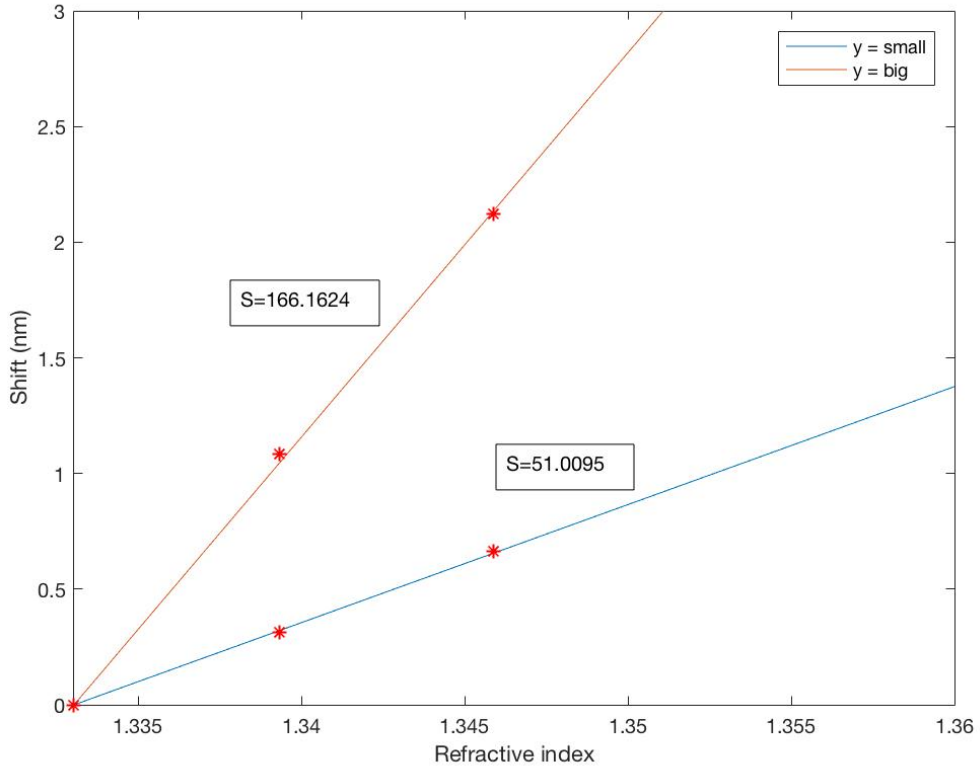

Figure 41: The BRIS measurement from experiment five, showing the sensitivites for both peaks.

Comparing the obtained decay lengths, 12.6497 nm and 26.3403 nm, with 15.1224 nm and 29.8749

nm that were used in the previous PLL/Si NPs experiment, there is some difference. The decay lengths used in the previous measurement were, as mentioned above, taken from the third POPC/DNA/Vesicle experiment. The main difference between these experiments was that in the fifth, a new sensor - albeit with the same composition and fabricated using the same procedure - was used. The decay lengths are intrinsic for a sensor, and thus it is no surprise that they are different. Still, a difference in decay lengths can be observed between experiments on the same sensor, and a more detailed analysis of this will be presented later in this section.

Moving on; after the POPC formation in figure 39, a series of plateaus are visible. A more clear picture of this can be seen in figure 42.

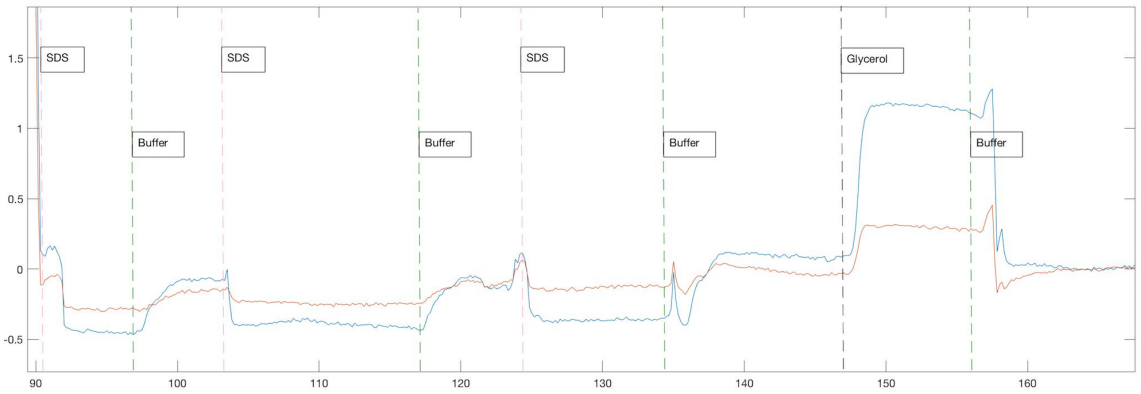

Figure 42: The shift plots during rinsing with SDS and buffer.

The noteworthy features of this part of the spectrum is the difference in baseline achieved with SDS and buffer. The SDS was initially used in order to remove the POPC bilayer, and as soon as this was done, the pumped solution was switched to buffer. However, the peak centroid shift increased by around 0.5 nm for the buffer, thus establishing a baseline higher than that before the POPC. As can be seen, the higher baseline established was the same each time buffer was being pumped, and this consistency prompts the conclusion that some residual POPC interacted with the sensor at these occasions. Lipid vesicle structure is heavily dependant on the ionic strength of the solution[50], and the buffer is indeed created for the purpose of stabilizing such biomolecules. SDS, however, seem to thoroughly remove any POPC still left in the system in the proximity of the sensor. These results indicates that a complete cleaning procedure - the removal of the sensor from the XNano and employment of both SDS and oxygen plasma - is necessary in order for the results to be as accurate as possible. This effect, the redshift to due to residual POPC, may also have interfered with prior experiments.

The thickness derived from the fifth experiment is shown in figure 43. As is apparent, a large portion of the spectrum is void - data points that are either 0 or extremely large. The cause of this, atleast for the Si NPs, is the very large ratio obtained. Looking at around 250 minutes in figure 39, the ratio between the large peak and the small peak is larger than 5. The ratio is, through the masterplot, translated into thickness. The ratio is shown in figure 44 and the masterplot is in figure 45.

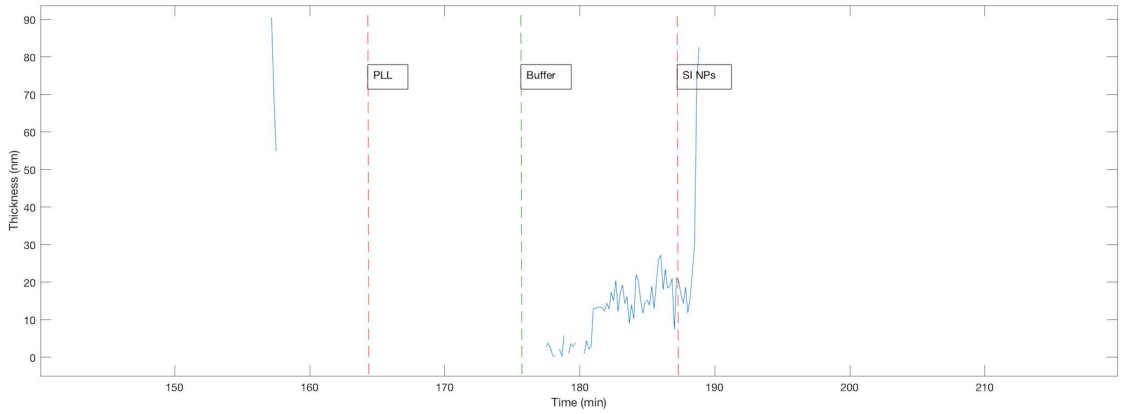

Figure 43: The thickness derived from the fifth experiment, displaying large portions of void - data points that are either 0 or close to infinite - in the spectrum.

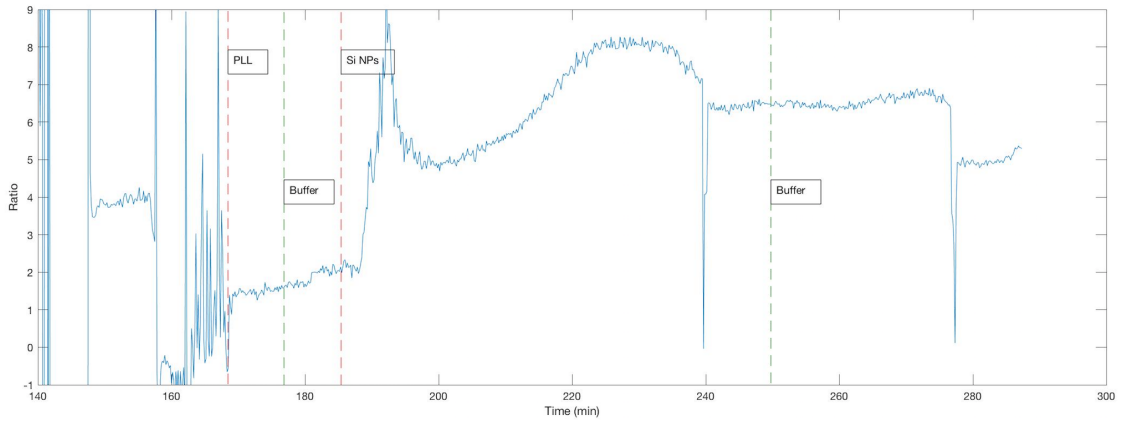

Figure 44: The ratio from experiment five, highlighting the main features.

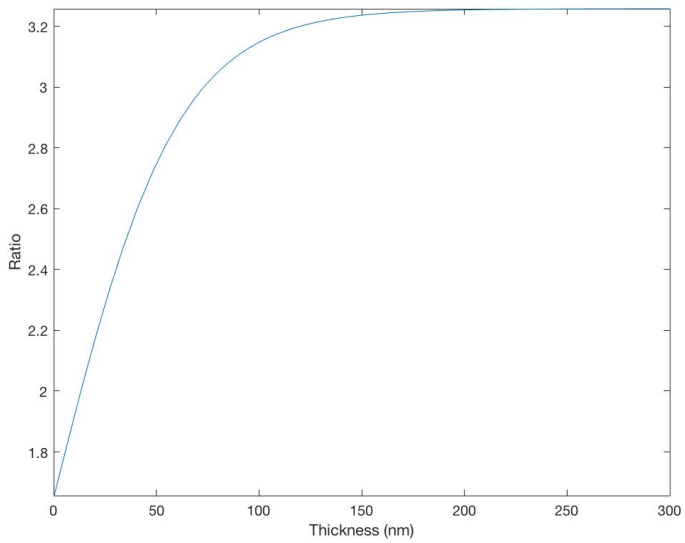

Figure 45: The masterplot from experiment five, displaying the relationship between the ratio of the shift plots to the thickness, as produced by the sensitivites and the decay lengths.

As is visible in the masterplot 45, ratios higher than 3.2 results in extremely high thicknesses, and even higher than that is practically undefined. The problem with the thickness rendition is therefore grounded in the sensitivites, the decay lengths or the shifts. The masterplot is created using equation (35), and is clearly dependant on the three mentioned parameters. Looking at figure 44, the ratio is well above 6 for the most part of the Si NP addition, but is at the end lowered. If this developement - the decrease of ratio with time - would be consequential throughout the experiment is hard to say, but in order to test it, the experiment should be run for longer time with buffer being added to the already established PLL/Si NP system. Since both sensitivities and decay lengths were of similar to previous experiments, it is probable that the problem with the thickness rendition does not lie in those parameters, but the actual shift plots. A possible physiochemical problem in this experiment lies with silica particles; perhaps they bind to each other, and thus creates a non-uniform layer on top of the PLL. This would indeed result in a very high thickness.

The sensitivities and decay lengths have varied throughout the experiments, and a compilation of the parameter values as determined from the measurements can be seen in table 3. The values, even though dissimilar, still adhere to certain trends; the sensitivity for the small peak is around 40 nm/RIU, and between 140 and 170 nm/RIU for the big peak. Moreover, the decay lengths exhibits a similar pattern. The presence of distinct trends is assuring, as it points to some robustness in the system. Even so; a variability of these parameters between experiments does not neccessarily entail bad results, since the final thickness as a function of time of the whole system is calibrated using these.

Experiment	1	2	3	4	5
BRIS	Small: 39.1380 Big: 167.2174	Small: 47.8547 Big: 168.9186	Small: 43.5926 Big: 141.7687	Small: 47.7561 Big: 140.9214	Small: 51.0095 Big: 166.1624
Decay length	Small: 13.6176 Big: 28.2241	Small: 12.9265 Big: 25.559	Small: 10.6354 Big: 21.1378	Small: - Big: -	Small: 15.1224 Big: 29.8749

Table 3: Sensitivites (in nm/RIU) and decay lengths (in nm) for all experiments.

5 Conclusion and Outlook

The nanoplasmonic dual-size ruler has been tested on two different molecular systems. The first system - POPC/DNA/Vesicles - produced data with a noise of around 0.5 nm, which is relatively good considering considering the small scale. How accurate the final results are with respect to the thickness determination is hard to tell. The thickness in the second experiment was around 13 nm, while the real size of only the spherical vesicles were 65 nm. However, keeping in mind that the vesicles are hollow, this might indeed be a good result. If it is, though, is dependent upon how long the DNA molecules are, and how they are arranged on the surface. The second system - PLL/Si NPs - produced worse results, providing unstable data and pointing at thicknesses way beyond the detection limit. A common feature in both of these systems is that the final thicknesses lies outside of the decay lengths for both peaks, and thus to further improve the sensor, nanodisks of higher decay lengths should be synthesized.

What the bad results stem from is hard to say, but when looking at the data, the largest problem does not seem to be the error, but the dynamics - the chemistry - of the systems studied. As was discussed in the previous section, it is the ratio of shift plots that have the most impact on the thickness. How the two disk sizes, the small and the big, reacts to the species adsorbed is naturally critical for the results, and if the problem lies here, it has to be solved in the fabrication step of the sensor. Alas, the fabrication of the sensor is one of the main areas through which the noise can be reduced. The difference in the parameter values between experiments might also have an impact on the results. The difference is perhaps due to difference in cleanliness of both the glass slide and the sensor prior to measurement. Perhaps fouling affect the two peaks asymmetrically, and thus produce the skew of the ratio that leads to strange thicknesses. To avoid this, a consistent cleaning regime has to be employed.

The main contribution to the noise in these experiments are, according to [17], due to excessive oxide around the sensor, and hence the fabrication step is probably the best way to deal with the remaining noise. Another way to generally improve the experiment is to be very careful not to introduce bubbles in the system. The best way to do this, as gathered through these experiments, is to use the pump in pushing mode as opposed to suction mode, since the latter seem to introduce more air into the system. Furthermore, finding a setup where decay length and BRIS can be determined throughout the experiment, perhaps by something that can be deposited in between steps that are of known thickness, would increase the accuracy.

It is appropriate to make a distinction between *qualitative* and *quantitative* experimental results. Even though the thickness determination is still not satisfying, a structural change such as that of the kink representing the rupture and formation of POPC is is in itself a proof-of-concept that the presented sensor is capable of register conformational and structural changes. This is important, since one of the applications envisioned for this sensor is the ability to monitor for example thermodynamics and kinetics, and for this to be possible, qualitative changes in the spectrum needs to be visible. Since the sensor has been shown to adequately record a structural change within a lipid membrane, the main conclusion of this thesis is as follows: the best way to further demonstrate the function of the dual-size ruler is to apply it in an even simpler system, preferably POPC together with one molecule that does not behave like DNA, i.e. that does not have the ability to be slanted when adsorbed to the lipid bilayer. The capability to determine if DNA is slanted or standing straight is one of the goals with the sensor, but in order to know if this is even possible to record with it, a simpler test system should be employed, e.g. a spherically symmetrical nanoparticle deposited on top of POPC.

References

[1] Encyclopaedia Britannica. *Metric system*, accessed 06.03.2018. https://www.britannica.com/topic/Treaty-of-the-Metre.

[2] Grégory Guisbiers, Sergio Mejía-Rosales, and Francis Leonard Deepak. Nanomaterial properties: size and shape dependencies. *Journal of Nanomaterials*, 2012, 2012.

[3] Kwangjin An and Gabor A Somorjai. Size and shape control of metal nanoparticles for reaction selectivity in catalysis. *ChemCatChem*, 4(10):1512–1524, 2012.

[4] Kaitlin M Bratlie, Hyunjoo Lee, Kyriakos Komvopoulos, Peidong Yang, and Gabor A Somorjai. Platinum nanoparticle shape effects on benzene hydrogenation selectivity. *Nano letters*, 7(10):3097–3101, 2007.

[5] Daniela Pozzi, Valentina Colapicchioni, Giulio Caracciolo, Susy Piovesana, Anna Laura Capriotti, Sara Palchetti, Stefania De Grossi, Anna Riccioli, Heinz Amenitsch, and Aldo Laganà. Effect of polyethyleneglycol (peg) chain length on the bio–nano-interactions between pegylated lipid nanoparticles and biological fluids: from nanostructure to uptake in cancer cells. *Nanoscale*, 6(5):2782–2792, 2014.

[6] SH Jo, Y Tu, ZP Huang, DL Carnahan, DZ Wang, and ZF Ren. Effect of length and spacing of vertically aligned carbon nanotubes on field emission properties. *Applied Physics Letters*, 82(20):3520–3522, 2003.

[7] JM Pitarke, VM Silkin, EV Chulkov, and PM Echenique. Theory of surface plasmons and surface-plasmon polaritons. *Reports on progress in physics*, 70(1):1, 2006.

[8] Mark I Stockman. Nanoplasmonics: past, present, and glimpse into future. *Optics express*, 19(22):22029–22106, 2011.

[9] Gustav Mie. Beiträge zur optik trüber medien, speziell kolloidaler metallösungen. *Annalen der physik*, 330(3):377–445, 1908.

[10] Alexandre Dmitriev. *Nanoplasmonic sensors*. Springer Science & Business Media, 2012.

[11] Magnus P Jonsson, Andreas B Dahlin, Laurent Feuz, Sarunas Petronis, and Fredrik Höök. Locally functionalized short-range ordered nanoplasmonic pores for bioanalytical sensing. *Analytical chemistry*, 82(5):2087–2094, 2010.

[12] Ferry Anggoro Ardy Nugroho, Rickard Frost, Tomasz J Antosiewicz, Joachim Fritzsche, Elin M Larsson Langhammer, and Christoph Langhammer. Topographically flat nanoplasmonic sensor chips for biosensing and materials science. *ACS sensors*, 2(1):119–127, 2016.

[13] EM Southern. Measurement of dna length by gel electrophoresis. *Analytical biochemistry*, 100(2):319–323, 1979.

[14] Simone Schröder, Asita Brandmüller, Xi Deng, Aftab Ahmed, and Hermann Wätzig. Improving precision in gel electrophoresis by stepwisely decreasing variance components. *Journal of pharmaceutical and biomedical analysis*, 50(3):320–327, 2009.

[15] DV Sheglov, SS Kosolobov, LI Fedina, EE Rodyakina, AK Gutakovskii, SV Sitnikov, AS Kozhukhov, SA Zagarskikh, VV Kopytov, VI Evgrafov, et al. High-precision nanoscale length measurement. *Nanotechnologies in Russia*, 8(7-8):518–531, 2013.

[16] Alyson V Whitney, Jeffrey W Elam, Shengli Zou, Alex V Zinovev, Peter C Stair, George C Schatz, and Richard P Van Duyne. Localized surface plasmon resonance nanosensor: a high-resolution distance-dependence study using atomic layer deposition. *The Journal of Physical Chemistry B*, 109(43):20522–20528, 2005.

[17] Padraic O'Reilly. Development of a nanoplasmonic ruler. 2017.

[18] Juri Ito and Kotaro Kajikawa. Measurement of molecular length of self-assembled monolayer probed by localized surface plasmon resonance. In *Organic Photonic Materials and Devices XVIII*, volume 9745, page 97450T. International Society for Optics and Photonics, 2016.

[19] Aditi Das, Jing Zhao, George C Schatz, Stephen G Sligar, and Richard P Van Duyne. Screening of type i and ii drug binding to human cytochrome p450-3a4 in nanodiscs by localized surface plasmon resonance spectroscopy. *Analytical chemistry*, 81(10):3754–3759, 2009.

[20] Jeffrey N Anker, W Paige Hall, Olga Lyandres, Nilam C Shah, Jing Zhao, and Richard P Van Duyne. Biosensing with plasmonic nanosensors. *Nature materials*, 7(6):442, 2008.

[21] Seung-Woo Lee, Kyeong-Seok Lee, Junhyoung Ahn, Jae-Jong Lee, Min-Gon Kim, and Yong-Beom Shin. Highly sensitive biosensing using arrays of plasmonic au nanodisks realized by nanoimprint lithography. *ACS nano*, 5(2):897–904, 2011.

[22] Wen Chen, Shunping Zhang, Qian Deng, and Hongxing Xu. Probing of sub-picometer vertical differential resolutions using cavity plasmons. *Nature communications*, 9(1):801, 2018.

[23] Deborah LM Rupert, Ganesh V Shelke, Gustav Emilsson, Virginia Claudio, Stephan Block, Cecilia Lässer, Andreas Dahlin, Jan O Lötvall, Marta Bally, Vladimir P Zhdanov, et al. Dual-wavelength surface plasmon resonance for determining the size and concentration of sub-populations of extracellular vesicles. *Analytical chemistry*, 88(20):9980–9988, 2016.

[24] Ferry AA Nugroho, Amaia Diaz de Zerio Mendaza, Camilla Lindqvist, Tomasz J Antosiewicz, Christian Müller, and Christoph Langhammer. Plasmonic nanospectroscopy for thermal analysis of organic semiconductor thin films. *Analytical chemistry*, 89(4):2575–2582, 2017.

[25] David Pines and David Bohm. A collective description of electron interactions: Ii. collective vs individual particle aspects of the interactions. *Physical Review*, 85(2):338, 1952.

[26] Arnold Sommerfeld. Zur elektronentheorie der metalle auf grund der fermischen statistik. *Zeitschrift für Physik*, 47(1-2):1–32, 1928.

[27] Stefan Alexander Maier. *Plasmonics: fundamentals and applications*. Springer Science & Business Media, 2007.

[28] William L Barnes. Particle plasmons: Why shape matters. *arXiv preprint arXiv:1609.04184*, 2016.

[29] Alessandro Alabastri, Salvatore Tuccio, Andrea Giugni, Andrea Toma, Carlo Liberale, Gobind Das, Francesco De Angelis, Enzo Di Fabrizio, and Remo Proietti Zaccaria. Molding of plasmonic resonances in metallic nanostructures: Dependence of the non-linear electric permittivity on system size and temperature. *Materials*, 6(11):4879–4910, 2013.

[30] Mark I Stockman. Nanoplasmonics: The physics behind the applications. *Phys. Today*, 64(2):39–44, 2011.

[31] Linda S Jung, Charles T Campbell, Timothy M Chinowsky, Mimi N Mar, and Sinclair S Yee. Quantitative interpretation of the response of surface plasmon resonance sensors to adsorbed films. *Langmuir*, 14(19):5636–5648, 1998.

[32] Ferry AA Nugroho, Beniamino Iandolo, Jakob B Wagner, and Christoph Langhammer. Bottom-up nanofabrication of supported noble metal alloy nanoparticle arrays for plasmonics. *ACS nano*, 10(2):2871–2879, 2016.

[33] Na Liu, Martin Mesch, Thomas Weiss, Mario Hentschel, and Harald Giessen. Infrared perfect absorber and its application as plasmonic sensor. *Nano letters*, 10(7):2342–2348, 2010.

[34] Daniel Rodrigo, Odeta Limaj, Davide Janner, Dordaneh Etezadi, F Javier Garcia de Abajo, Valerio Pruneri, and Hatice Altug. Mid-infrared plasmonic biosensing with graphene. *Science*, 349(6244):165–168, 2015.

[35] Longhua Guo, Joshua A Jackman, Huang-Hao Yang, Peng Chen, Nam-Joon Cho, and Dong-Hwan Kim. Strategies for enhancing the sensitivity of plasmonic nanosensors. *Nano Today*, 10(2):213–239, 2015.

[36] Hyungsoon Im, Huilin Shao, Yong Il Park, Vanessa M Peterson, Cesar M Castro, Ralph Weissleder, and Hakho Lee. Label-free detection and molecular profiling of exosomes with a nano-plasmonic sensor. *Nature biotechnology*, 32(5):490, 2014.

[37] Stefan A Maier, Mark L Brongersma, Pieter G Kik, Scheffer Meltzer, Ari AG Requicha, and Harry A Atwater. Plasmonics—a route to nanoscale optical devices. *Advanced materials*, 13(19):1501–1505, 2001.

[38] Ujwol Palanchoke, Henning Kurz, Rodrigo Noriega, Sahar Arabi, Vladislav Jovanov, Philipp Magnus, Hasan Aftab, Alberto Salleo, Helmut Stiebig, and Dietmar Knipp. Tuning the plasmonic absorption of metal reflectors by zinc oxide nano particles: application in thin film solar cells. *Nano Energy*, 6:167–172, 2014.

[39] Amanda J Haes, Christy L Haynes, Adam D McFarland, George C Schatz, Richard P Van Duyne, and Shengli Zou. Plasmonic materials for surface-enhanced sensing and spectroscopy. *MRS bulletin*, 30(5):368–375, 2005.

[40] Vivian Kaixin Lin, Siew Lang Teo, Renaud Marty, Arnaud Arbouet, Christian Girard, Esther Alarcon-Llado, Shu Hua Liu, Ming Yong Han, Sudhiranjan Tripathy, and Adnen Mlayah. Dual wavelength sensing based on interacting gold nanodisk trimers. *Nanotechnology*, 21(30):305501, 2010.

[41] Magnus P Jonsson, Peter Jönsson, and Fredrik Höök. Simultaneous nanoplasmonic and quartz crystal microbalance sensing: Analysis of biomolecular conformational changes and quantification of the bound molecular mass. *Analytical chemistry*, 80(21):7988–7995, 2008.

[42] Andreas B Dahlin, Jonas O Tegenfeldt, and Fredrik Höök. Improving the instrumental resolution of sensors based on localized surface plasmon resonance. *Analytical chemistry*, 78(13):4416–4423, 2006.

[43] Paresh C Dave, Elvis K Tiburu, Krishnan Damodaran, and Gary A Lorigan. Investigating structural changes in the lipid bilayer upon insertion of the transmembrane domain of the membrane-bound protein phospholamban utilizing 31p and 2h solid-state nmr spectroscopy. *Biophysical journal*, 86(3):1564–1573, 2004.

[44] Alireza Mashaghi, Marcus Swann, Jonathan Popplewell, Marcus Textor, and Erik Reimhult. Optical anisotropy of supported lipid structures probed by waveguide spectroscopy and its application to study of supported lipid bilayer formation kinetics. *Analytical chemistry*, 80(10):3666–3676, 2008.

[45] Magnus P Jonsson, Peter Jönsson, Andreas B Dahlin, and Fredrik Höök. Supported lipid bilayer formation and lipid-membrane-mediated biorecognition reactions studied with a new nanoplasmonic sensor template. *Nano Letters*, 7(11):3462–3468, 2007.

[46] Anna Åkesson, Tania Lind, Nicky Ehrlich, Dimitrios Stamou, Hanna Wacklin, and Marité Cárdenas. Composition and structure of mixed phospholipid supported bilayers formed by popc and dppc. *Soft Matter*, 8(20):5658–5665, 2012.

[47] Limor Pasternak and Yaron Paz. Low-temperature direct bonding of silicon nitride to glass. *RSC Advances*, 8(4):2161–2172, 2018.

[48] Lars Hillered, Johann Valtysson, Per Enblad, and Lennart Persson. Interstitial glycerol as a marker for membrane phospholipid degradation in the acutely injured human brain. *Journal of Neurology, Neurosurgery & Psychiatry*, 64(4):486–491, 1998.

[49] Polysciences Inc. *Colloidal silica microspheres*, accessed 24.05.2018. http://www.polysciences.com/default/silica-microspheres-005956m-colloidal.

[50] Edwin Kalb, Sammy Frey, and Lukas K Tamm. Formation of supported planar bilayers by fusion of vesicles to supported phospholipid monolayers. *Biochimica et Biophysica Acta (BBA)-Biomembranes*, 1103(2):307–316, 1992.